

Metal Halide Perovskite Arrays: From Construction to Optoelectronic Applications

Xun Han, Wenqiang Wu, Hao Chen, Dengfeng Peng, Li Qiu,* Peiguang Yan,* and Caofeng Pan*

Inorganic semiconductor arrays revolutionize many areas of electronics, optoelectronics with the properties of multifunctionality and large-scale integration. Metal halide perovskites are emerging as candidates for next-generation optoelectronic devices due to their excellent optoelectronic properties, ease of processing, and compatibility with flexible substrates. To date, a series of patterning technologies have been applied to perovskites to realize array configurations and nano/microstructured surfaces to further improve device performances. Herein, various construction methods for perovskite crystal or thin film arrays are summarized. The optoelectronic applications of the perovskite arrays are also discussed, in particular, for photodetectors, light-emitting diodes, lasers, and nanogratings.

1. Introduction

Metal halide perovskites have emerged as a class of semiconductor materials with superior optoelectronic properties, including high absorption coefficients,^[1] long carrier diffusion length,^[2] low trap densities,^[3] efficient photoluminescence (PL), and broad emission range.^[4] These impressive properties make them potential candidates for high-performance optoelectronic devices, such as photovoltaics,^[5] photodetectors,^[6] lasers,^[7] and light-emitting diodes (LEDs).^[8] Since the first perovskite solar cell was reported in 2009,^[9] the power conversion efficiencies have realized an evolution from 3.8 to a certified 25.2%.^[10] The external quantum efficiency (EQE) of LEDs also experiences an encouraging improvement from 8.5%^[11] to exceeding 20%

in the green light emission in the past six years.^[12] Metal halide perovskite possesses a general chemical formula of ABX_3 , in which A is a cation, B is a metal, and X is a halide. Typically, the A site is a monovalent cation (e.g., methylammonium ($CH_3NH_3^+$, MA^+), formamidinium ($NH_2CHNH_2^+$, FA^+), or Cs^+), the B site is a divalent metal cation (e.g., Pb^{2+} or Sn^{2+}), and the X site is a halide anion (e.g., Cl^- , Br^- , or I^-). The 12-fold coordinated A-site cations are located in the middle of a 3D network that is surrounded by eight corner-shared $[BX_6]^{4-}$ octahedra. This crystal structure of perovskite provides

them vastly unique physics and chemistry.^[13]

Recently, various optimizations have focused on the thin perovskite films to improve device performance, such as morphology engineering for large grain size,^[14] controlled single-crystalline film growth,^[15] and substitution of Pb with nontoxic ions,^[16] which accelerate the commercialization progress of these devices. In addition, inspired by the patterning technology of conventional inorganic semiconductor, e.g., silicon,^[17] carbon nanotubes,^[18] graphene,^[19] group II–VI and III–V compounds,^[20] to optimize the parameters of various devices, the optical and optoelectronic characteristics of perovskite have demonstrated to be improved through forming novel nano/microstructures on the surface of perovskites or constructing perovskite arrays.^[21] Given the soft nature of perovskite materials,^[22] conventional photolithography, consisting of photoresist spin-coating, baking, and developing, which is most common in the current semiconductor industry, can cause decomposition of perovskites.^[23] Nondestructive patterning technologies are necessary to be developed for the perovskite arrays. As early as 2001, Kagan et al. demonstrated a microcontact printing method for layered $(C_6H_5C_2H_4NH_3)_2SnI_4$ thin film array with a resolution of $\approx 3 \mu m$.^[24] The thin-film transistor based on the perovskite arrays exhibited improved performance of low operational voltage and no leakage current. In 2003, Cheng et al. adopted capillary force lithography to synthesize the $(C_6H_5C_2H_4NH_3)_2PbI_4$ stripe arrays with various widths of 0.8, 15, and $50 \mu m$ with strong green fluorescence.^[25] Subsequently, a series of growth methods for perovskite arrays as well as exciting array devices have been explored, exhibiting potentially unique opportunities for integrated optoelectronics.

This review covers the recent progress of perovskite arrays of both single crystals and polycrystalline thin films, with a focus on the construction method and their optoelectronic applications. We discuss four major array growth methods, which

Dr. X. Han, Prof. L. Qiu
College of Mechatronics and Control Engineering
Shenzhen University
Shenzhen 518060, China
E-mail: qili@szu.edu.cn

W. Wu, Prof. C. Pan
CAS Center for Excellence in Nanoscience
Beijing Key Laboratory of Micro-nano Energy and Sensor
Beijing Institute of Nanoenergy and Nanosystems
Chinese Academy of Sciences
Beijing 100083, P. R. China
E-mail: cfpan@binn.cas.cn

H. Chen, Prof. D. Peng, Prof. P. Yan, Prof. C. Pan
College of Physics and Optoelectronic Engineering
Shenzhen University
Shenzhen 518060, China
E-mail: yanpg@szu.edu.cn

 The ORCID identification number(s) for the author(s) of this article can be found under <https://doi.org/10.1002/adfm.202005230>.

DOI: 10.1002/adfm.202005230

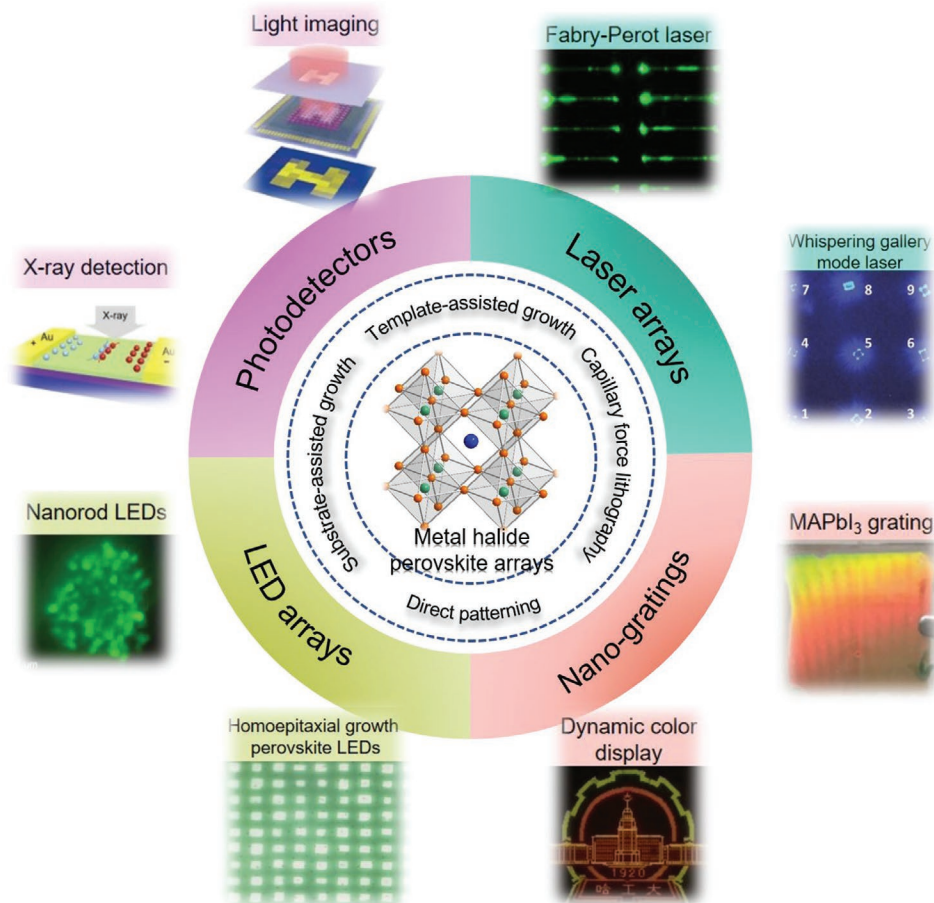


Figure 1. Schematic illustration showing four methods for the construction of the perovskite arrays and their optoelectronic applications.

are template-assisted growth, substrate-assisted growth, capillary force-assisted growth, and direct patterning technologies (Figure 1). We summarize their applications in photodetector arrays, LED arrays, laser arrays, and nanogratings as well as device architectures therein. Finally, we propose some future prospects regarding the development of the perovskite arrays and integrated optoelectronics.

2. Construction of Perovskite Arrays

According to the operation procedures, we summarize the construction methods of perovskite arrays in four categories: template-assisted growth, substrate-assisted growth, capillary force-assisted growth, and direct patterning technologies. The first three growth methods are classified to the bottom-up synthesis strategy. In this strategy, the geometrical confinement of precursors was formed through the template, prepatterned substrate, or capillary force to complete the patterning process before the perovskite synthesis. Specifically, template-assisted growth requires various facile templates, e.g., polydimethylsiloxane (PDMS), anodized aluminum oxide (AAO), specified roller and photoresist patterns, etc., to physically separate the precursor solution or metal nanoclusters. Substrate-assisted growth relies on the prepatterned substrates by using a special treatment to generate area where is favorable to precursor distribution. Capillary force-assisted growth utilizes capillary bridge

and trailing to achieve precursor solution domain array followed by solvent evaporation and perovskite crystallization. The fourth growth method is a typical top-down fabrication strategy which achieves patterns on the as-fabricated perovskite film by the micromachining, including modified etching and printing processes. Generally, the bottom-up synthesis strategy possesses complicated and time-consuming procedures, however, it can establish precise control on the growth process to improve crystalline quality. For example, through regulating the solvent evaporation rate, large-scale single-crystal perovskite arrays were achieved through the PDMS template and capillary force-assisted growth method. On the contrary, the top-down fabrication strategy could perform patterning process on the perovskite film directly and demonstrate advantages of effective control on the resolution, dimension, and alignment of the perovskite arrays. A comparison of perovskite arrays with various fabrication strategies and material properties is summarized in Table 1.

2.1. Geometrically Confined Growth

2.1.1. PDMS Template-Assisted Patterning

PDMS template is one of the most commonly used templates for the growth of organic semiconductor arrays due to its high hydrophobicity and good thermal and oxidative stability.^[26]

Table 1. Summary of the fabrication strategies and material properties of the perovskite arrays. (FTO: fluorine-doped tin oxide; ITO: indium tin oxide; QD: quantum dot; Y = “Yes”; N = “No”).

Materials	Growth method	Substrate	Growth area	Morphology	Single crystal	Crystal structure	Dimensions			Space [μm]	Ref.
							Length [μm]	Width [μm]	Height [μm]		
MAPbBr ₃	PDMS template-assisted	Si or glass	1 cm × 1 cm	Nanowire	N	Cubic	10–50	0.46–2.5	0.08–1	10	[27]
(BA) ₂ (MA) _{n-1} Pb _n I _{3n+1} (n = 1–8)				Microring	N	Ruddlesden–Popper	12, 19, 29 (diameter)	2.5	1.6		[29]
CsPbCl _{3-x} Br _x (x = 0, 1, 2, 3)		SiO ₂ /Si	1 cm × 1 cm	Microplate	Y	Orthorhombic	2.5 ± 0.3	2.5 ± 0.3	0.6 ± 0.2	20	[28]
CsPbBr ₃		SiO ₂ /Si		Microwire	Y	Orthorhombic	500	2.5–8.6	2.4–8.2	200	[31]
MAPbI ₃	AAO template-assisted	AAO	3 cm × 3 cm	Vertically aligned nanowire	Y	Cubic			2		[37]
CsPbBr ₃			2 cm ²		Y	Cubic		0.2–0.25	1	0.5	[39]
MASnI ₃					Y	Cubic		0.25		0.5	[36]
MAPbI ₃	Roller-assisted	SiO ₂ /Si	4 in. wafer	Thin film stripe	Y	Tetragonal		10	0.2	0.4	[44]
MAPbI ₃	Blade-assisted	SiO ₂ /Si or PET	1 cm × 1 cm	Microwire	Y	Tetragonal		2–3			[46]
MAPbI ₃	Modified photolithography	FTO glass		Thin film with various patterns	N				0.225		[48]
MAPbBr ₃		FTO glass		Microplate	Y	Cubic			3	≈30	[50]
CsPbBr ₃		Si	Large area	QD thin film	N					≈0.3	[51]
PEA-CsPbX ₃ (X = Cl, Br, I)		Si or ITO glass	4 in. wafer	Thin film with various patterns	N						[53]
MAPbI ₃	Surface-functionalized substrate-assisted	SiO ₂ /Si	Wafer scale	Microplate	Y	Tetragonal	≈10	≈10	0.3–0.5		[56]
MAPbI ₃		Si	Wafer scale	Microplate	Y	Tetragonal	15 (edge length)		0.2		[57]
MAPbI _{3-x} Cl _x		PET	6 cm × 6 cm	Thin film	N	Tetragonal	100	100		400	[55]
CsPbX ₃ (X = Cl, Br)	Surface-guided	Mica		Nanowire	Y	Cubic	0.16	0.03	0.015		[59]
CsPbBr ₃		Sapphire		Nanowire	Y	Cubic					[60]
MAPbBr ₃	Capillary bridge lithography	Glass		Microplate	Y	Cubic	3.6–4.1	3.6–4.1	0.9 ± 0.1	20	[63]
(BA) ₂ (MA) _{n-1} Pb _n I _{3n+1} (n = 2–5)		Glass		Nanowire	Y	Ruddlesden–Popper		0.4–10.5	0.15–1.5	2–10	[64]
MAPb(I _{1-x} Br _x) ₃ (x = 0–0.4)	Capillary trailing lithography	SiO ₂ /Si		Nanowire	Y	Tetragonal		0.4 ± 0.03			[67]
CsPbBr ₃		SiO ₂ /Si		Nanowire	Y	Cubic		0.51	0.2	5	[66]
MAPbX ₃ (X = Cl, Br)	Nanoimprinting	SiO ₂ /Si	≈4 cm ²	Film with line, square, and hexagon patterns	N	Cubic (MAPbBr ₃), tetragonal (MAPbI ₃)		0.4	0.15	0.4	[69]
MAPbI ₃		ITO glass	1.7 cm × 1.7 cm	Grating	N				0.1–0.12		[70]
MAPbBr ₃	FIB etching			Grating				0.1368		0.1207	[72]
MAPbBr ₃	ICP etching			Grating				0.25	0.205	0.1	[74]

Table 1. Continued.

Materials	Growth method	Substrate	Growth area	Morphology	Single crystal	Crystal structure	Dimensions			Space [μm]	Ref.
							Length [μm]	Width [μm]	Height [μm]		
MAPbBr ₃	Inkjet printing	Si	Wafer scale	Microplate	Y	Cubic	6.5–7.3	6.5–7.3			[76]
CsPbBr ₃		SiO ₂ /Si or PET	4 in. wafer	QD thin film	N	Cubic					[78]
MAPbBr ₃	Laser-induced growth	Glass with metal		Thin film	N	Cubic					[80]
CsPbBr ₃		Inside the transparent medium		QD	N						[84]

To achieve various perovskite patterns, the PDMS template provides the space confinement for the precursor solution to form liquid domains and can be removed after solvent evaporation. Liu demonstrated a PDMS template-confined solution

growth (PTCSG) method for MAPbBr₃ nanowire (NW) arrays, as shown in **Figure 2a**.^[27] First, a PDMS template with rectangular grooves was fabricated through the soft lithography on a Si substrate. Then, the PDMS template was placed on a stock

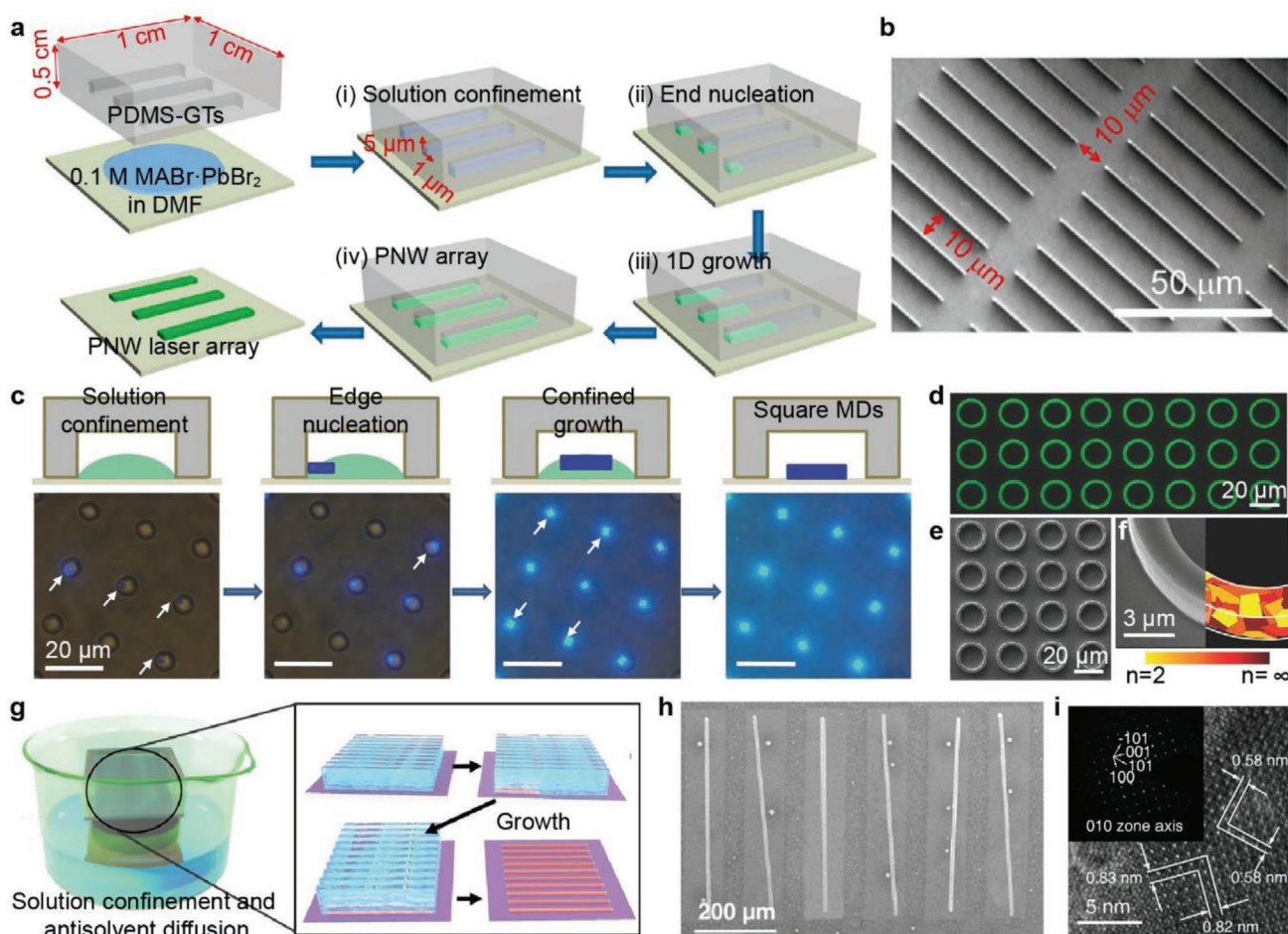


Figure 2. a) Schematic illustration showing the method of PDMS template confined solution growth of MAPbBr₃ nanowire arrays. b) SEM images of MAPbBr₃ nanowire arrays. a,b) Reproduced with permission.^[27] Copyright 2017, American Chemical Society. c) In situ monitoring growth status of CsPbCl₃ microdisk arrays. Reproduced with permission.^[28] Copyright 2017, Wiley-VCH. d,e) Low-magnification fluorescence microscopy image and SEM image of Ruddlesden–Popper perovskites ($n = 6$) microring arrays. f) High-magnification SEM image of a single microring and schematic illustration showing multiphase in the microrings. d–f) Reproduced with permission.^[29] Copyright 2018, Wiley-VCH. g) Preparation schematic of the CsPbBr₃ microwire arrays with the assist of antisolvent. h) SEM image and i) high-resolution TEM image of CsPbBr₃ microwire showing the [010] zone axis. g–i) Reproduced with permission.^[31] Copyright 2019, Wiley-VCH.

precursor solution of MABr and PbBr₂ in N,N-dimethylformamide (DMF) on a target substrate with a hydrophilic surface. By applying mild pressure (<20 kPa) on the PDMS template, the solution was driven into the rectangular grooves. As slow evaporation of DMF (about 2–3 h), the nucleation of perovskite first occurred at the end position of groove, and then grew up rapidly along this groove. After the solvent evaporated completely, the PDMS template was peeled off, leaving MAPbBr₃ NW arrays on the target substrate. As shown in the scanning electron microscopy (SEM) images of MAPbBr₃ NWs (Figure 2b), the MAPbBr₃ NWs are well-aligned and uniformly distributed on the substrate with the width of around 460 nm and length of 50 μm. By using different templates with various lengths of rectangular grooves, MAPbBr₃ NW arrays with length varied from 10 to 50 μm were prepared. Furthermore, the width and height of NWs can also be controlled by the width of grooves and the concentration of the stock solution, respectively. In addition, through changing the shape of grooves inside the PDMS pad, square CsPbCl₃ microdisk arrays (Figure 2c)^[28] and 2D Ruddlesden–Popper perovskites (RPPs) microring arrays (Figure 2d)^[29] were formed on the target substrate. To reveal the growth process of the array, the in situ observation of the CsPbCl₃ microdisk arrays was conducted through fluorescence microscopy (Figure 2c). Similar to the NW growth process in Figure 2a, as slow evaporation of DMF (about 2–3 h), blue fluorescence spot gradually appeared at the edge position of grooves of PDMS, which indicates the nucleation of perovskite. Then the primary nuclei moved to the center position of PDMS grooves and grew up rapidly (within 10 min) into square microdisk, which showing strong blue fluorescence. The PTCSG method is versatile and can also be applied to the growth of 2D RPPs ((BA)₂(MA)_{n-1}Pb_nBr_{3n+1}) arrays. The fluorescence microscopy image (Figure 2d) and SEM image (Figure 2e) demonstrate a large-scale microring array with uniform dimensions and precise position fabricated by this method. Each microring exhibits smooth outer surfaces and sharp edges and composes multiphased quantum well (Figure 2f). The phase impurity of 2D perovskites is also an immediate issue that needs to be addressed, which often increases the defect density.

The antisolvent-assisted crystallization method is a powerful tool to realize high-performance perovskite solar cells.^[30] Yang et al. modified the PTCSG method by introducing CH₃CN as an antisolvent for the growth of monocryalline CsPbBr₃ microwire (MW) arrays (Figure 2g).^[31] After pressing the PDMS template on the stock solution, they placed the system into a sealed dish containing 300 mL of CH₃CN for 24 h. During this process, CH₃CN diffused into the stock solution leading to the crystallization of CsPbBr₃ MWs. The as-fabricated MWs exhibit smooth surface, sharp edges, and uniform width of 2.6 μm and height of 2.5 μm (Figure 2h). Crystalline structure was investigated through high-resolution transmission electron microscope (HRTEM) and selected area electron diffraction (SAED) (Figure 2i). These results prove the orthorhombic structured MW with the [010] zone axis. Such a growth method protects the perovskite from directly contacting with the moisture environment and provides control on the crystallization process to improve the crystalline quality. However, there is a challenge in the alignment between PDMS template and prepatterned sample, which limits its application in the pixel-addressable device arrays.

2.1.2. AAO Template-Assisted Patterning

AAO template with spatially discrete, tunable, and oriented nanopores is widely used for nanomaterials growth through electrodeposition, such as inorganic semiconductors,^[32] metals,^[33] and polymers.^[34] Recently, Ashley et al. developed the uniform CH₃NH₃PbI₃, CH₃NH₃PbBr₃, and Cs₂SnI₆ NW arrays based on AAO templates.^[35] They adopted the facilitated one-step method which is to inject perovskite solution into the nanopores of the AAO template and followed by a short annealing step. Gu et al. also formed a 3D perovskite NW arrays based on AAO templates via a novel vapor-solid-solid reaction.^[36] Figure 3a demonstrates the procedures of AAO template-assisted growth of 3D perovskite NW arrays. This method started with two-step anodization of high-purity Al foil for AAO template preparation. Then, the barrier layer at the bottom of the AAO template was thinned down by a voltage-ramping-down process and followed by the electrochemical deposition of Pb or Sn nanoclusters at the bottom of AAO channels. Then, Al substrate was etched away for freestanding AAO template preparation. Finally, the 3D perovskite NW array was formed through the reaction between Pb or Sn nanoclusters and MAI vapor in a tube furnace. The backscattered electron (BSE) mode SEM images of Pb nanoclusters and MAPbI₃ NWs proved this vapor-solid-solid reaction. Pb nanoclusters were successfully deposited at the bottom of AAO channels (Figure 3bi) before NW growth, and then the reaction was confined in the channels for vertically aligned NW array growth (Figure 3b).^[37] In addition, by changing the combinations of metal nanoclusters and vapors, various kinds of perovskite NWs can be synthesized through this method.^[38] For example, the CsPbI₃ NW arrays were fabricated through the reaction between Pb nanoclusters and CsI vapor (Figure 3c,d).^[39] The CsPbI₃ NWs are cubic in nature with an interplanar spacing of 0.236 nm which corresponds to the distance between two neighboring (211) planes of cubic structure (Figure 3e). It is worth noting that the length of the NW synthesized via this vapor-solid-solid reaction can be controlled by the amount of Pb nanoclusters and the reaction time. In addition, the stability of NW samples exhibits dramatic improvement compared with the planar film samples due to the protection of AAO template sidewalls.^[36] As shown in Figure 3f, the decomposition of perovskite is attributed to the reaction between water molecules, oxygen, and perovskite materials. The sidewalls of the AAO template can block lateral diffusion of water and oxygen molecules, only leaving the vertical diffusion path for these molecules, thus leading to a slow decomposition rate of perovskite materials. MASnI₃ NW arrays and planar films were synthesized to demonstrate this protection phenomenon. The two kinds of samples were exposed to the air with 70% humidity for 0, 1, and 7 d after fabrication for the stability comparison. For the NW sample, the photoluminescence (PL) peak intensity remained almost the same after 1 d (Day 2), subsequently experienced 35% degradation after 7 d (Day 8) (Figure 3g). However, the PL intensity of film samples exhibited a cliff-like drop after 12 min in air, while taking 7 d for NW samples to decay down to the same level, indicating the enhanced moisture resistivity of the NW samples (Figure 3h). Furthermore, semitransparent and nanopillar-structured perovskite solar cell was demonstrated based on the

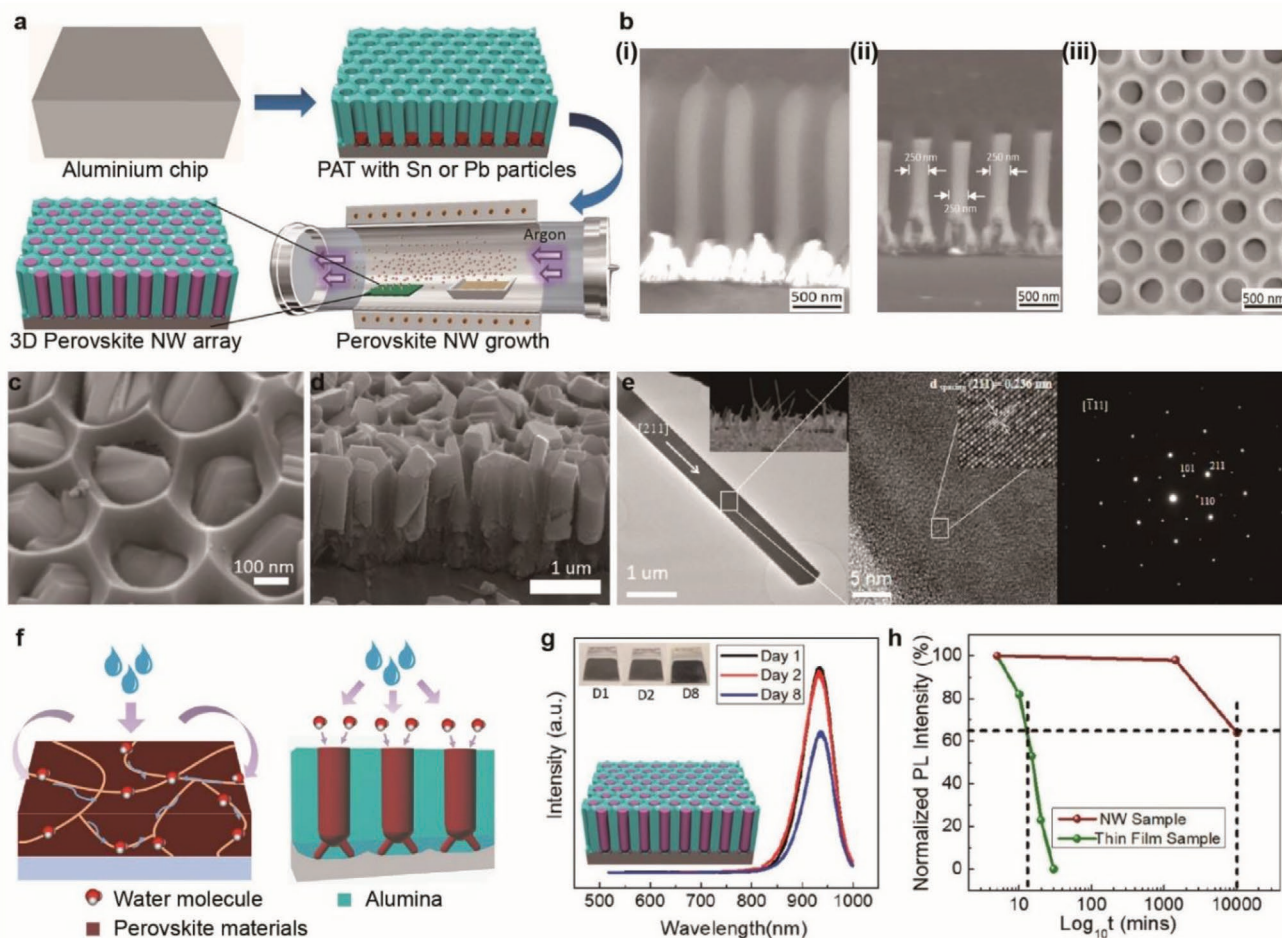


Figure 3. a) Schematic illustration of AAO template-assisted growth of 3D perovskite NW arrays. Reproduced with permission.^[36] Copyright 2016, American Chemical Society. b) SEM images of i) Pb particles before NW growth, and ii) cross-section view and iii) top view of MAPbI₃ NWs after growth in the AAO template. Reproduced with permission.^[37] Copyright 2016, Wiley-VCH. c) Top view and d) cross-section view of as-synthesized CsPbI₃ NWs in the AAO template. e) TEM image, high-resolution TEM image, and SAED pattern of CsPbI₃ NW showing the [111] zone axis. c–e) Reproduced with permission.^[39] Copyright 2017, American Chemical Society. f) Comparison of planar film sample and NWs sample in moisture showing the sidewall protection effect of the AAO template. g) PL emission spectra of MASnI₃ NWs after exposing to air with 70% humidity for 0 (after growth), 1 and 7 d (insets are optical images of NW sample in the air). h) Normalized PL emission spectra from planar thin film sample and NW sample. f–h) Reproduced with permission.^[36] Copyright 2016, American Chemical Society.

AAO template.^[40] Benefitting from the ion migration suppression of nanopillar structure, the solar cell exhibits impressive long-term stability compared with planar devices.

2.1.3. Roller and Blade Printing

Solution-based hot-casting technology has been widely used to improve the crystal quality of perovskite by heating the substrate to accelerate the crystal growth processes.^[41] Nie et al. employed this method to develop millimeter-scale grains of perovskite for high-efficiency solar cells.^[42] Epitaxial lateral growth is a method for high-quality single-crystal semiconductor film synthesis by using geometrical confinement and kinetic control to restrict of crystal growth in the vertical direction.^[43] Inspired by these two technologies, Lee et al. reported a solution-based roller printing method to produce wafer-scale single-crystal patterned perovskite thin films (Figure 4a).^[44]

First, a cylindrical metal roller was wrapped up with a PDMS mold with periodic patterns. Then, an ink supplier filled with MAPbI₃ precursor was mounted with the metal roller and subsequently was placed in contact with a preheated substrate. The perovskite crystal was crystallizing immediately as the solvent evaporation caused by the hot substrate. With the movement of the roller, the seed crystals grew rapidly via instant crystallization in the lateral direction, while vertical growth was blocked by the roller. The geometrical confinement in the vertical direction can prevent the misaligned growth of seed crystals, resulting in the growth of the single-crystal thin film with the tetragonal crystal structure. This process involves print process of precursors and kinetic control of the perovskite crystallization process, which makes it facile for the fabrication of large-scale, uniform, high crystalline quality stripe arrays. A patterned 3 × 3 in. perovskite thin film was demonstrated on a 4 in. wafer through this method (Figure 4b). The large-scale film consisted of a unidirectional array of parallel strips with a

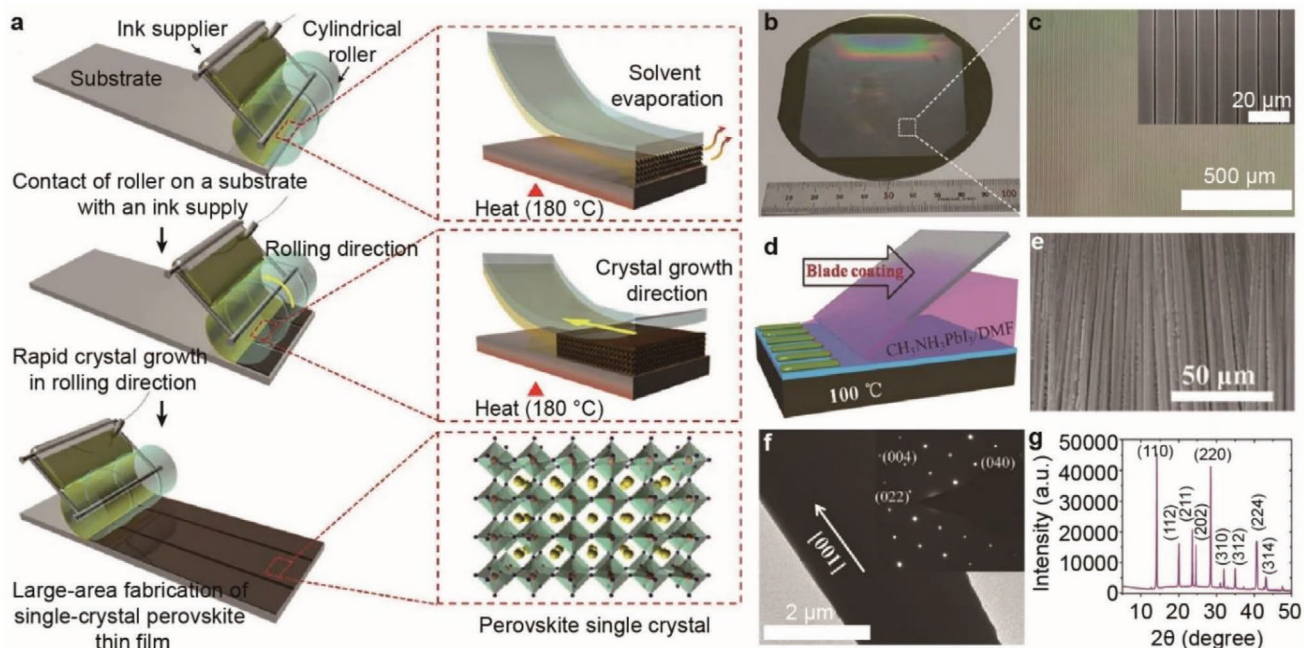


Figure 4. a) Lateral growth of patterned single-crystal MAPbI₃ film. Left panel: schematic of the fabrication process for MAPbI₃ film with a rolling mold. Right panel: solvent evaporation and crystallization occurred at the end of the channel. b) Photographic image of the 3 × 3 in. MAPbI₃ film fabricated on a 4 in. Si/SiO₂ wafer. c) Enlarged view of the patterned MAPbI₃ film. Inset is the SEM image of 10 μm-wide MAPbI₃ stripes with a 400 nm-wide gap. a–c) Reproduced with permission.^[44] Copyright 2017, Nature Publishing Group. d) Lateral growth of MAPbI₃ microwire arrays using the blade coating process. e) SEM image of the MAPbI₃ microwire arrays. f) TEM image of the MAPbI₃ microwire and corresponding SAED pattern. g) XRD image of the MAPbI₃ microwire arrays. d–g) Reproduced with permission.^[46] Copyright 2016, Wiley-VCH.

width of 10 μm and 400 nm-wide gaps (Figure 4c). The dimensions of these strips were consistent with those patterns on the PDMS mold, leading to a highly controllable patterned perovskite thin film.

Compared with the thin perovskite film, 1D perovskite micro/nanostructure exhibits unique advantages in device applications.^[45] A simple blade coating method was developed for the growth of 1D single-crystalline MAPbI₃ MWs (Figure 4d).^[46] With a blade dragging the MAPbI₃ precursor solution across a heated substrate, highly oriented MAPbI₃ MWs were formed with length up to centimeter scale. The MWs were straight and well-aligned with a uniform width of 2–3 μm and the smooth top surface (Figure 4e). The HRTEM image and SAED pattern (Figure 4f) demonstrated that the MWs are single-crystalline and X-ray diffraction (XRD) results (Figure 4g) indicated a tetragonal perovskite structure of the MWs.

2.1.4. Modified Photolithography

Conventional electron-beam lithography and photolithography, including baking, exposure, and development, are most easily accessible and powerful tools in the semiconductor industry for micro/nanopatterning.^[47] However, these high-resolution lithography approaches cannot be directly applied to the perovskite materials due to the solubility in polar solvents and poor thermal stability.^[48] Wu et al. modified the conventional photolithography method by employing poly(4-butylphenyl-diphenyl-amine) (poly-TPD) as the auxiliary layer to achieve

the perovskite arrays (Figure 5a).^[49] This process started with the poly-TPD layer spin-coating on the substrate followed by a conventional photolithography process to pattern the poly-TPD layer. Subsequently, the photoresist was lifted-off in DMF solution leaving a patterned poly-TPD layer on the substrate. A precursor solution of lead acetate (Pb(Ac)₂) and methylammonium iodide (MAI) in DMF was spin-coated on the as-fabricated substrate to form perovskite films inside the poly-TPD pattern. Finally, the poly-TPD auxiliary layer was removed by chlorobenzene (CB) spin-drop-casting. Compared with the abovementioned methods with fixed template, the modified photolithography could provide high-resolution and complex patterns as well as excellent alignment with other prepatterned samples. By combining with the growth dynamics control, it will demonstrate potential application in the fabrication of large-scale, uniform, and integrated optoelectronic device arrays. The as-fabricated perovskite films were composed of close-packing small grains without pinholes uniformly distributing on the substrate (Figure 5b). Benefitting from the conventional photolithography process, arbitrarily shaped complex patterns with clear edges can be achieved through this approach (Figure 5c). Furthermore, the Ostwald ripening process can be applied for the formation of single-crystalline perovskite crystals.^[50] Wu et al. demonstrated an Ostwald ripening assisted photolithography (ORAP) process to fabricate single-crystalline MAPbBr₃ microplate arrays.^[51] By optimizing the isopropanol concentration, a large crystal with few small crystals was formed in one pixel through the as-mentioned poly-TPD approach. Then, the array was placed into the DMF

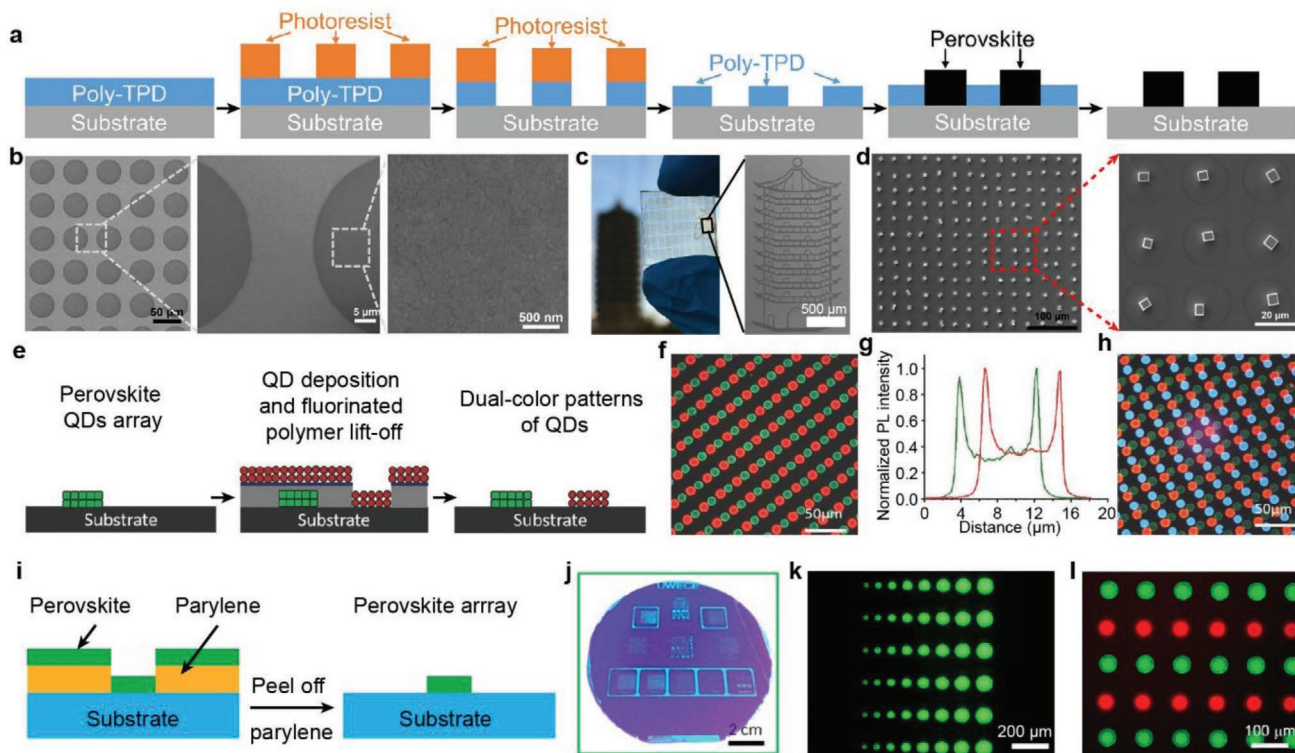


Figure 5. a) Schematic illustration of the growth of patterned MAPbI₃ with poly-TPD as the auxiliary layer. b) SEM images of MAPbI₃ film with the circle pattern. c) Photograph and SEM images of MAPbI₃ film with the tower-shape pattern. a–c) Reproduced with permission.^[49] Copyright 2017, American Chemical Society. d) SEM images of single-crystalline MAPbBr₃ microplate arrays fabricated through an additional Ostwald ripening assisted crystallization process. Reproduced with permission.^[51] Copyright 2018, American Chemical Society. e) Schematic illustration showing the fabrication of QD arrays with dual-color pattern by using orthogonal lithography twice. f) Fluorescent image of the dual-color QD pattern and g) corresponding spatial distribution PL spectra. h) Fluorescent image of the advanced RGB pattern. e–h) Reproduced with permission.^[52] Copyright 2018, Wiley-VCH. i) Schematic illustration showing the fabrication of perovskite film array through parylene peeling off strategy. j) Optical image of the patterned perovskite film on a 4 in. wafer under UV lamp excitation. k) Fluorescent image of the green perovskite circles with diameters ranging from 20 to 90 μm. l) Fluorescent image of the dual-color perovskite pattern. i–l) Reproduced with permission.^[53] Copyright 2020, American Chemical Society.

atmosphere with a certain concentration to only deliquesce the small crystals. According to the Ostwald ripening theory, the small crystals will be recrystallized on the large crystal. Thus, the single-crystalline microplate was achieved by repeating the Ostwald ripening process for 1–3 cycles. The MAPbBr₃ microplate arrays demonstrated good uniformity, smooth surface, and clear edges (Figure 5d).

To fully utilize the advantage of optical precision of conventional photolithography, Lin et al. developed a novel orthogonal lithography process for large-scale arrays with multicolor (binary and ternary emission) pixels.^[52] They utilized the fluorinated polymer and stripper to break the limitation from polar-nonpolar solvents thus realizing the CsPbBr₃ quantum dots (QDs) patterning. Then the same orthogonal lithography process was performed to produce red-emitting CdSe/Cd_{1-x}Zn_xSe_{1-y}S_y QDs right beside the green-emitting CsPbBr₃ QDs (Figure 5e). The high-resolution fluorescent image shows the micropixel arrays consisting of binary pixels of red and green QD circles with a resolution of ≈1000 ppi (Figure 5f). The spatial distribution of PL intensity for both green and red pixels showed a nest-like shape with the PL intensity in the middle region is ≈30–40% of the maximum PL

intensity at the rim (Figure 5g). Intriguingly, by performing this approach thirdly, blue-emitting CdSe/Cd_{1-x}Zn_xSe_{1-y}S_y QDs can be integrated into the binary pixels to form an RGB array (Figure 5h).

In the orthogonal lithography process, using appropriate orthogonal solvents to remove photoresist is a critical step to avoid decomposition of perovskite arrays. To address the incompatibility between perovskites and solvents, Zou et al. developed a dry lift-off approach based on the poor adhesion between parylene-C film and substrate for patterning perovskite arrays photolithographically in micrometer resolution.^[53] A desired pattern was formed on the parylene-C film through the standard photolithography and reactive ion etching (RIE) process, followed by perovskite precursor spin-coating and crystallization. Then, the parylene-C film was easily peeled off, leaving the perovskite film array on the substrate (Figure 5i). The large-scale perovskite film with various patterns and dimensions can be achieved through this protocol (Figure 5j,k). The minimum feature of the perovskite array can reach as small as 4 μm. By performing the patterning process twice, the green and red perovskite arrays could be formed on the substrate sequentially (Figure 5l).

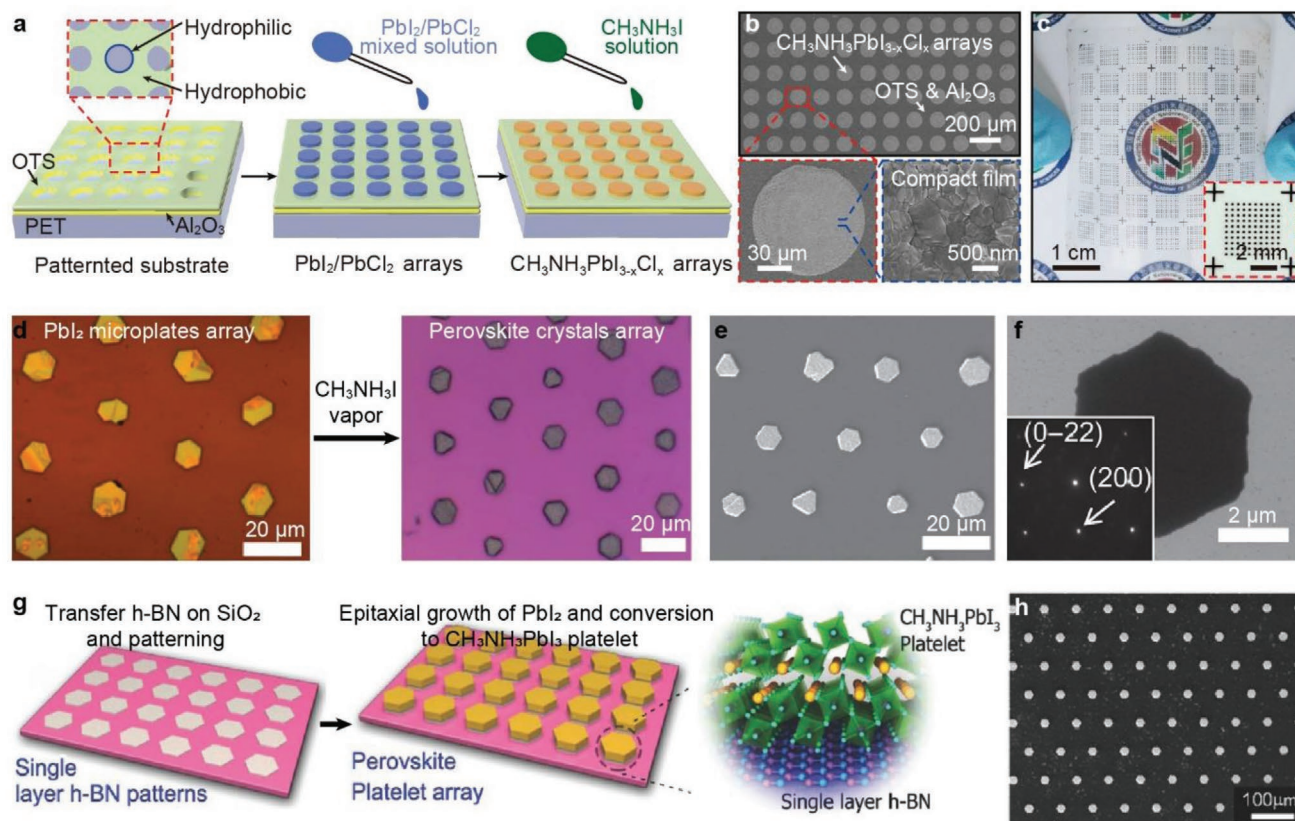


Figure 6. a) Schematic illustration of the solution-based growth method of patterned $\text{MAPbI}_{3-x}\text{Cl}_x$ film on a surface-functionalized PET substrate. b) SEM image of patterned $\text{MAPbI}_{3-x}\text{Cl}_x$ film and magnified SEM images showing the compact film surface. c) Photograph of large-scale $\text{MAPbI}_{3-x}\text{Cl}_x$ film array on PET substrate. a–c) Reproduced with permission.^[56] Copyright 2018, Wiley-VCH. d) Conversion of PbI_2 microplates to MAPbI_3 crystal arrays under MAI vapor. e) SEM image of MAPbI_3 microplate arrays. f) TEM image and SAED pattern of a MAPbI_3 microplate. d–f) Reproduced with permission.^[57] Copyright 2015, American Association for the Advancement of Science. g) Schematic illustration of the fabrication MAPbI_3 microplate arrays on the prepatterned BN films. h) SEM images of MAPbI_3 microplates array. g, h) Reproduced with permission.^[58] Copyright 2016, Wiley-VCH.

2.2. Substrate-Assisted Growth

2.2.1. Surface-Functionalized Substrate-Assisted Growth

Since the superior chemical stability, the deposition and control strategy of PbX_2 is versatile,^[54] uniform patterned PbX_2 layer can be easily obtained. Two-step growth of perovskite materials can be modified for array growth, which is using the surface-functionalized substrate for PbX_2 array deposition and followed by conversion to perovskite.^[55] Wu et al. reported a two-step growth method of $\text{MAPbI}_{3-x}\text{Cl}_x$ film arrays on a prepatterned substrate.^[56] A patterned substrate was firstly prepared by the treatment with (octadecyl)trichlorosilane (OTS) and oxygen plasma, resulting in a hydrophobic surface where hydrophilic sites are periodically distributed (Figure 6a). Then, a mixed solution of PbI_2 and PbCl_2 was spin-coated on the as-prepared substrate and the thin solution film was only trapped in the hydrophilic regions to allow subsequent nucleation of $\text{PbI}_2/\text{PbCl}_2$ crystals. Finally, the MAI solution was spin-coated on the $\text{PbI}_2/\text{PbCl}_2$ arrays to convert precursor arrays to $\text{MAPbI}_{3-x}\text{Cl}_x$ film arrays, followed by an annealing step to improve the crystallization process. A critical step of this method is to simply spin-coat perovskite precursor on the prepatterned substrate

and the resolution of arrays, the dimension and shape of pixels can be tuned by the hydrophilic areas on the substrate. All these features make this method to be cost-effective, fast, suitable for large-scale fabrication, and compatible with various solution-processed semiconductors. The $\text{MAPbI}_{3-x}\text{Cl}_x$ film arrays exhibited clear and uniform shapes with compact surfaces (Figure 6b). Large-scale $\text{MAPbI}_{3-x}\text{Cl}_x$ film arrays with rectangle shape and complex patterns proved that the approach was versatile (Figure 6c). Wang et al. developed a single-crystalline MAPbI_3 microplate array based on the surface-functionalized substrate.^[57] They achieved the PbI_2 seed arrays on a patterned substrate by dragging dilute PbI_2 solution across the substrate surface and then seeded substrate was immersed into a saturated PbI_2 solution for further PbI_2 microplate arrays formation. Then, the PbI_2 microplate arrays converted into MAPbI_3 crystal arrays under MAI vapor in a tube furnace at 120 °C (Figure 6d). During the conversion process, the overall locations of crystals almost remained the same and the morphology of the final array was determined by the PbI_2 microplate due to the controllability of the reaction (Figure 6e). The SAED pattern of a perovskite crystal showed a single set of diffraction spots which is indexed to the tetragonal structure (Figure 6f). In addition to patterning by an assembled monolayer of hydrophobic

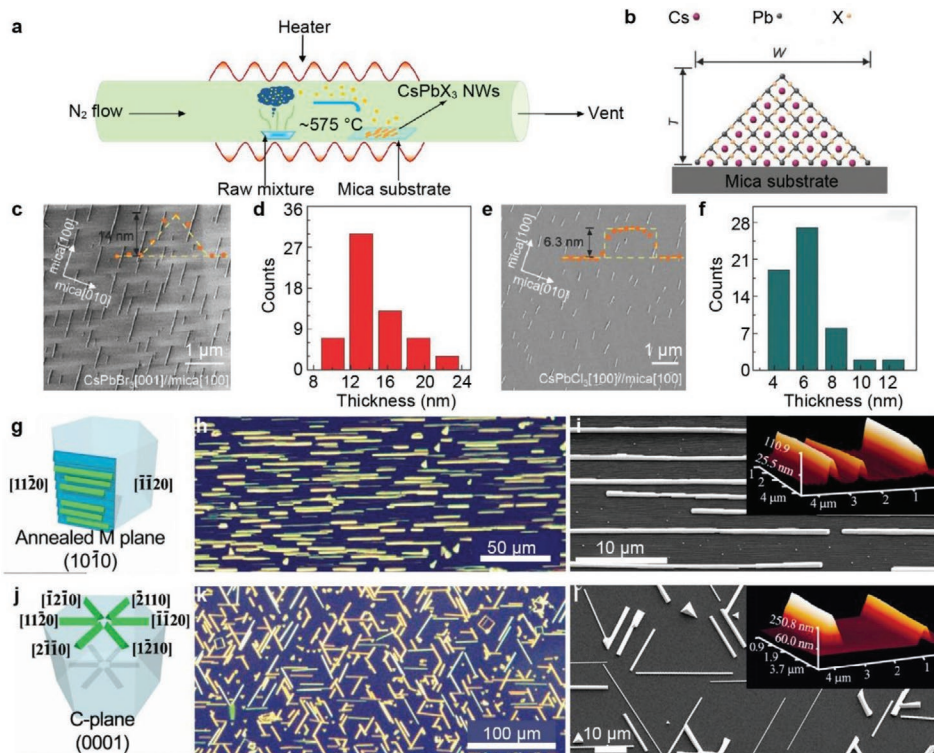


Figure 7. a) Schematic illustration of the growth process of the CsPbX_3 NW arrays. b) Schematic illustration of the cross-section view of a NW on the mica substrate. c) SEM images of the CsPbBr_3 NW arrays. Inset is the height profile of an individual NW. d) Thickness statistics of CsPbBr_3 NW arrays in an area of $6.2 \times 6.2 \mu\text{m}^2$. e) SEM images of the CsPbCl_3 NW arrays. Inset is the height profile of an individual NW. f) Thickness statistics of CsPbCl_3 NW arrays in an area of $10 \times 10 \mu\text{m}^2$. a–f) Reproduced with permission.^[59] Copyright 2018, Wiley-VCH. Schematic illustration of the g) graphoepitaxial and j) epitaxial growth mode of the CsPbBr_3 NWs on the sapphire substrate. h) Dark-field optical image and i) SEM image of CsPbBr_3 NWs obtained through graphoepitaxial growth mode. Inset is the AFM image of graphoepitaxial CsPbBr_3 NWs. k) Dark-field optical image and l) SEM image of CsPbBr_3 NWs obtained through epitaxial growth mode. Inset is the AFM image of epitaxial CsPbBr_3 NWs. g–l) Reproduced with permission.^[60] Copyright 2018, American Chemical Society.

OTS, a buffer layer of single-layer hexagonal boron nitride (h-BN) can be employed to synthesize the patterned perovskites (Figure 6g).^[58] In this method, the single-layer h-BN can be served not only as an intermediate layer to provide nuclei sites but also as a cladding layer in lasing and an insulating dielectric layer in the electric device due to its wide bandgap. The MAPbI_3 microplate arrays were only formed in the area covered by the h-BN layer with controllable shape and thickness (Figure 6h).

2.2.2. Surface-Guided Nanowire Growth

The perovskite NWs can be synthesized by the noncatalyzed vapor-solid (VS) growth mechanism. Through utilizing specific substrates, the growth direction of perovskite NWs can be regulated. Gao et al. demonstrated the CsPbX_3 ($X = \text{Br}, \text{Cl}$) NWs array with strong emission anisotropy via van der Waals incommensurate epitaxy on the muscovite mica substrate.^[59] The NW array was synthesized through a single chemical vapor deposition (CVD) method (Figure 7a). CsX and PbX_2 powders were mixed with molar ratio 1:1 as the precursors and freshly cleaved mica was used as the target substrate. The synthesis procedures were carried out at 575°C for CsPbBr_3 and 620°C for CsPbCl_3 with the N_2 flow under the pressure of 50 Torr for CsPbBr_3 and

100 Torr for CsPbCl_3 . The structure of CsPbX_3 NW grown on the mica substrate is shown in Figure 7b. Both the CsPbBr_3 and CsPbCl_3 NWs were well aligned along one direction on the mica substrate (Figure 7c,e). The CsPbBr_3 NWs demonstrated a triangular cross section with the top corner angle of $\approx 90^\circ$ (inset, Figure 7c), indicating the cubic phase of the NW. The average thickness of the CsPbBr_3 NW counted in an area of $6.2 \times 6.2 \mu\text{m}^2$ was ≈ 15 nm (Figure 7d). Different from CsPbBr_3 NW, the CsPbCl_3 NW demonstrated a relatively small thickness of ≈ 7 nm (Figure 7f) and rectangular cross section (inset, Figure 7e), indicating the different epitaxial surfaces of two kinds of perovskite NW on the mica substrate. Oksenberg et al. reported the graphoepitaxial and epitaxial growth mode of the CsPbBr_3 NWs on the sapphire substrate.^[60] In the graphoepitaxial mode, the NWs grew along the nanogrooves on the annealed M-plane sapphire resulting in the alignment in one direction (Figure 7g,h). On the flat C-plane sapphire, the NWs grew along with six iso-periodic directions in the epitaxial growth mode (Figure 7j,k). All the NWs in the two modes demonstrated a triangular cross section and grew along with the [001] crystallographic orientation of the cubic phase CsPbBr_3 . By controlling the growth conditions, the height of NWs was ranging from 20 nm to a few micrometers and the typical length of NWs was a few tens of micrometers (Figure 7i,l). The CVD method without a

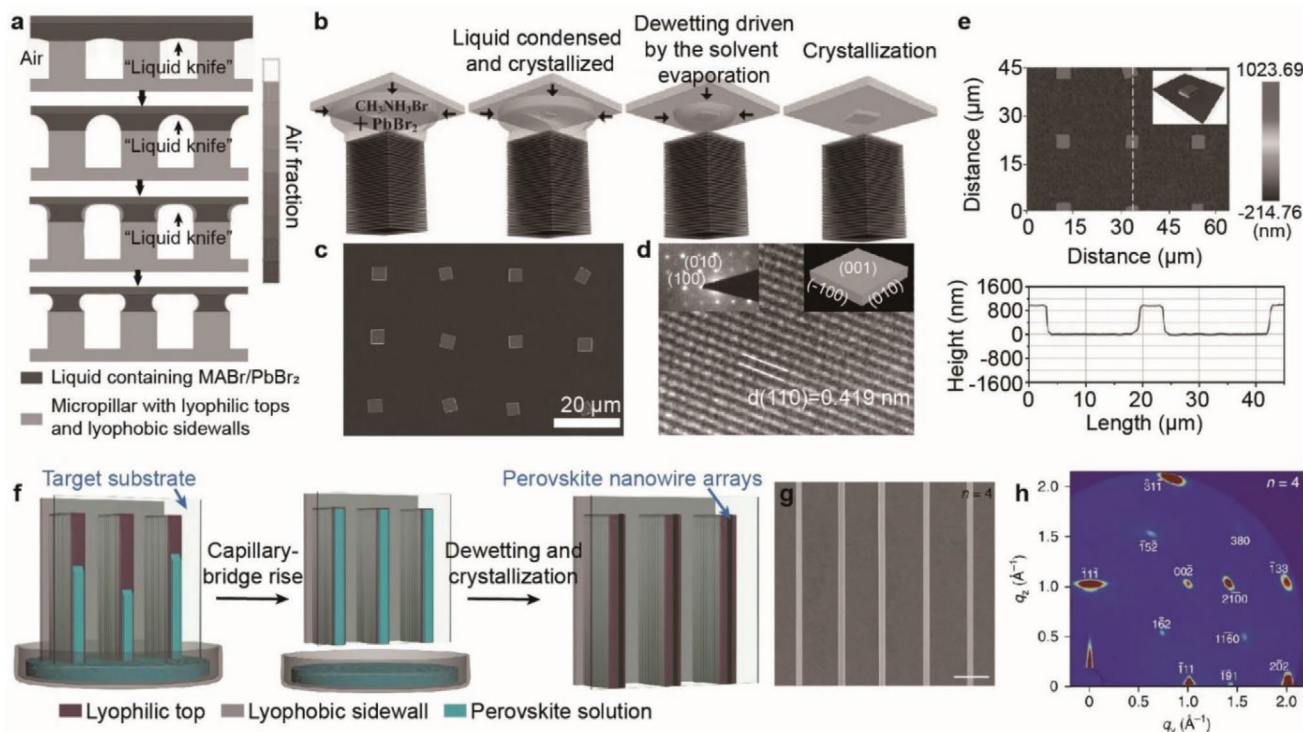


Figure 8. a) Computational fluid dynamics simulation of the dewetting process among the micropillars. b) Schematic illustration of the fabrication process of a single MAPbBr₃ microplate. c) SEM image of MAPbBr₃ microplate arrays. d) High-resolution TEM image showing a set of orthogonal planes. Inset is the SAED pattern of a MAPbBr₃ plate. e) 3D surface topographic image of the MAPbBr₃ microplate arrays. a–e) Reproduced with permission.^[64] Copyright 2016, Wiley-VCH. f) Schematic illustration of the 2D-perovskite NW arrays fabrication process by capillary-bridge rise method. g) SEM image of 2D perovskite NW arrays ($n = 4$). h) Grazing incidence wide-angle X-ray scattering pattern of 2D perovskite nanowires ($n = 4$). f–h) Reproduced with permission.^[65] Copyright 2018, Nature Publishing Group.

deliberate artificial pattern could provide a facile strategy for the perovskite NW arrays fabrication.

2.3. Capillary Force-Assisted Growth

2.3.1. Capillary Bridge Lithography

Capillary bridge is a ubiquitous phenomenon observed between two neighboring solid surfaces in nature.^[61] Pokroy et al. demonstrated the self-organization of mesoscale bristles into ordered, hierarchical helical assemblies, which is driven by the capillary force.^[62] Feng et al. employed the capillary bridge to pattern micrometer-sized droplets with controlled dimensions and positions, yielding patterned organic crystal arrays.^[63] They modified this approach and achieved MAPbBr₃ microplate arrays with precise position and homogeneous size.^[64] The asymmetric-wettability micropillars with hydrophilic top and hydrophobic sidewalls were adopted to regulate the location and geometry of the capillary bridge. Upon contacting with perovskite solution on a target substrate, the top surface of micropillars was wetted by the liquid, forming a sandwich structure. Following slow evaporation of the solvent, the liquid film was split into isolated capillary bridges anchored on the top of micropillars (Figure 8a). With further evaporation, the nucleation and growth of perovskite occurred in the capillary bridge induced

by the increasing concentration of perovskite solution (Figure 8b). Finally, the micropillar template was peeled off to leave MAPbBr₃ microplate arrays on the target substrate. The MAPbBr₃ microplate arrays were in an ordered position with uniform square shape and sharp edges (Figure 8c). Crystalline information was obtained by TEM, showing a single set of diffraction spots which indicates cubic MAPbBr₃ perovskite structure (Figure 8d). A flat surface with a homogeneous height of ≈ 900 nm was demonstrated in a 3D surface topographic image (Figure 8e). Consequently, they designed a “capillary-bridge rise” assembly system based on a revised asymmetric-wettability Si template with rectangle pillars to fabricate the 2D RPP ((BA)₂(MA)_{*n*-1}Pb_{*n*}I_{3*n*+1}) NW arrays.^[65] When the system contacted with perovskite solution, the perovskite liquid rose inside the gap between micropillars and target substrate, driven by the capillary force and Laplace pressure, and yielded individual capillary bridges anchored on the pillar tops (Figure 8f). With annealing at 80 °C, the nucleus of 2D RPP generated and subsequently grew to NW arrays. The morphology of NW arrays is revealed in Figure 8g, demonstrating an array with strict alignment, homogenous width, and precise position. Grazing incidence wide-angle X-ray scattering (GIWAXS) analyses were performed to characterize the crystallography orientation of NWs (Figure 8h). The set of discrete diffraction spots in Figure 8h was attributed to the (101)-oriented 2D perovskite, indicating the single growth orientation of nanowires.

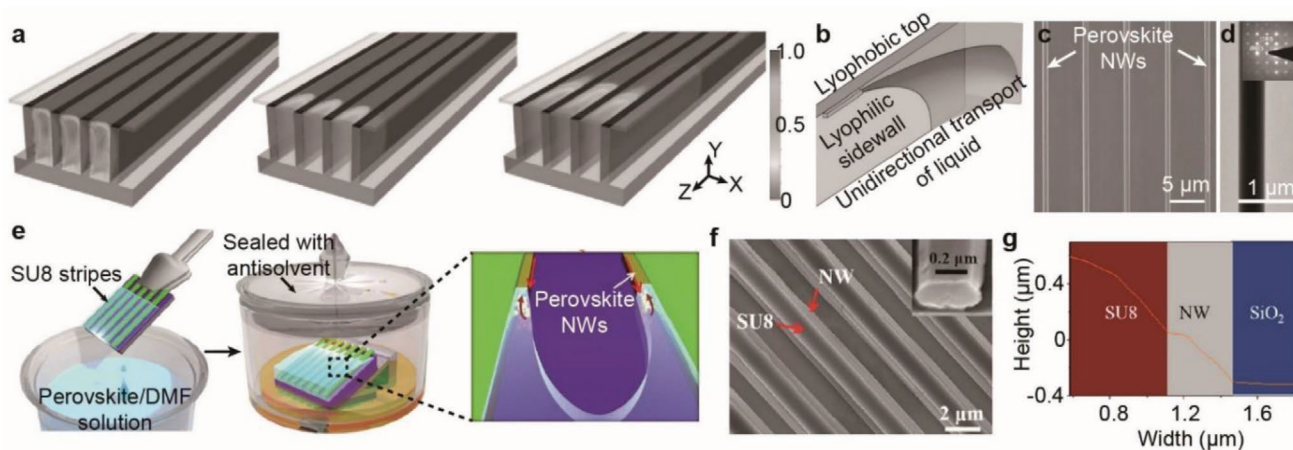


Figure 9. a) Computational fluid dynamics simulation of liquid flow confined between Si micropillar and the target substrate. b) Schematic illustration of the crystallization process of CsPbBr₃ NW along the lyophobic top. c) SEM image of CsPbBr₃ NW arrays. d) TEM image of a single NW. Inset is the SAED pattern. a–d) Reproduced with permission.^[67] Copyright 2017, Wiley-VCH. e) Schematic illustration of a fluid-guided antisolvent vapor-assisted crystallization method for the fabrication of MAPbI₃ NW arrays. f) SEM image of MAPbI₃ NW grown along the SU8 strips. Inset is the cross-section view of a MAPbI₃ NW. g) Height profile from the edge of SU8 stripes. e–g) Reproduced with permission.^[68] Copyright 2017, American Chemical Society.

2.3.2. Capillary Trailing Lithography

During the dewetting process in the asymmetric wettability system, a “capillary trailing” is formed at the hydrophilic and hydrophobic boundary regulated by the capillary force.^[66] CsPbBr₃ NW arrays have been achieved via the capillary trailing growth method.^[67] The simulation results showed that the liquid flow was confined between Si micropillars and the target substrate. With the liquid evaporation, capillary trailings were generated unidirectionally along the sidewalls (Figure 9a). As for perovskite solution in this system, crystal nucleation and continuing growth were accompanied by the receding capillary trailing. The bulk liquid in front of the crystallization site served as a mass supplier, making sure the concentration in the capillary trailing was supersaturated, to enable the continuing growth of NWs (Figure 9b). To evaluate the morphology and crystal structure of NWs, SEM and TEM were performed. The morphology of NW array is revealed in Figure 9c, showing strictly aligned NW arrays with homogeneous width on a SiO₂ substrate. A TEM image (Figure 9d) demonstrated a single NW with a clear boundary, and corresponding SAED pattern (inset, Figure 9d) illustrated a [100] growth orientation in the growth direction. Deng et al. adopted SU-8 photoresist stripes with nature hydrophobic surfaces on a hydrophilic SiO₂ substrate to construct the asymmetric wettability system for the growth of MAPbI₃ NW arrays (Figure 9e).^[68] In addition to the as-mentioned capillary trailing method, the saturated antisolvent (CH₂Cl₂) was employed to isolate perovskite from the air moisture, thus ensuring high crystal quality NWs. The SEM image in Figure 9f presented that the NWs grew along the two sides of SU-8 photoresist strips with a smooth surface and regular-shaped edge. The atomic force microscopy (AFM) image (Figure 9g) showed the height profile of NWs with a height of 300 nm and a width of 400 nm.

2.4. Direct Patterning Technologies

2.4.1. Nanoimprinting

Nanoimprinting technology has become an alternative to the conventional photolithography approach and has been applied to pattern standard semiconductor materials to obtain high ordered nanostructures for improving electronic and optoelectronic properties.^[69] Jeong et al. modified the conventional nanoimprinting, introducing a soft-gel state of perovskite solution, for patterning the MAPbBr₃ film (Figure 10a).^[70] Instead of DMF used in the aforementioned approaches, a high-boiling-point solvent, dimethyl sulfoxide (DMSO), was employed in this approach to prepare the perovskite solution. This gel-assisted imprinting approach started with spin-coating of perovskite solution on pretreated SiO₂/Si substrate, leaving the moldable gel state thin film due to the slow evaporation rate of DMSO (Figure 10a). Subsequently, a prepatterned PDMS mold was pressed gently on the gel state film to allow deformation of the film for pattern replication from PDMS mold. Finally, with the substrate being annealed at 80 °C, the precursor solution was converted into perovskite film, followed by PDMS mold peeling-off to complete this approach. A large-scale micropatterned MAPbBr₃ film was achieved with a uniform line width of 5 μm (Figure 10b). In addition, sub-microscale dimensions can also be demonstrated by this approach, shown in the topographic image in Figure 10c, with a width of 400 nm and a height of 150 nm. The morphology of line patterns is shown in Figure 10d,e, revealing the smooth surface without mechanical cracks and physical voids. Mao et al. reported a novel nanoimprinting method by forming a liquid-phase intermediate.^[71] A solid thin MAPbI₃ film was first prepared and was placed into the container filled with anhydrous methylamine (MA) vapor. The MA vapor penetrated into the solid film leading to a transparent liquid-phase intermediate (CH₃NH₃PbI₃·CH₃NH₂),

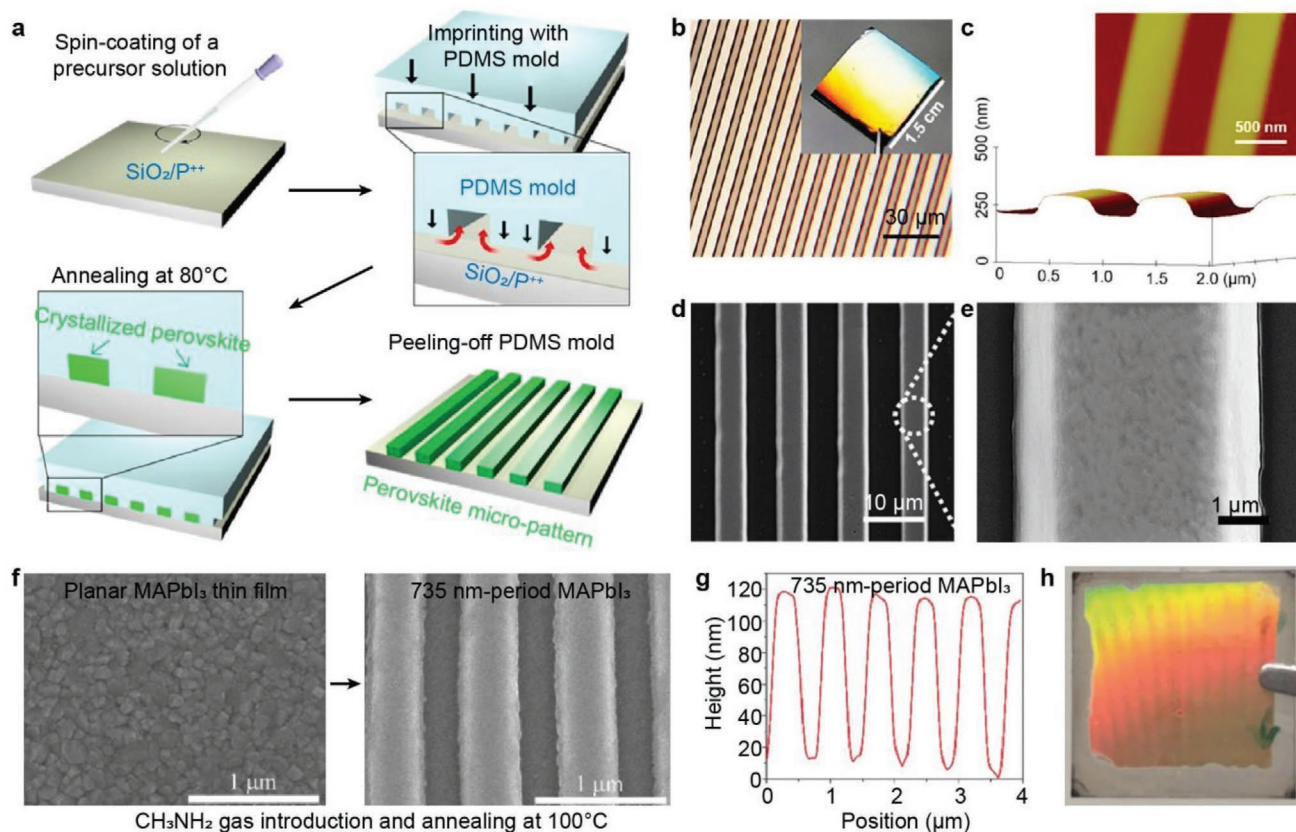


Figure 10. a) Schematic illustration of the solvent-assisted gel printing method for MAPbBr₃ film patterning. b) Optical image of MAPbBr₃ line patterns. Inset is the photograph of this pattern exhibiting light interference. c) 3D topographic and AFM image of MAPbBr₃ line patterns with a period of ≈800 nm. d) SEM image and e) a magnified SEM image of MAPbBr₃ line patterns. a–e) Reproduced with permission.^[70] Copyright 2016, American Chemical Society. f) Construction of MAPbBr₃ gratings from a planar thin film through the thermal nanoimprinting approach. g) Height profile and h) photograph of 735 nm period MAPbBr₃ gratings. f–h) Reproduced with permission.^[71] Copyright 2017, Wiley-VCH.

which was ready to deform to make close contact with PDMS mold. Then, the liquid intermediate returned to solid perovskite after leaving the MA vapor, followed by PDMS mold peeling-off. As shown in Figure 10f, the periodic-structured MAPbBr₃ demonstrated smoother surface and larger grain size than its thin film counterpart, which was attributed to the recrystallization through the phase transformation. The large area of nanostructured MAPbBr₃ film (Figure 10h) can also be demonstrated by this approach with uniform height and width (Figure 10g).

2.4.2. Focused Ion Beam (FIB) and Inductively Coupled Plasma (ICP) Etching

The FIB technology provides the capability of direct patterning on as-prepared films without assistance of template and mask, thus simplifying the fabrication procedures and minimizing the damage of materials during the patterning process. Alias et al. investigated the essential FIB etching parameters, for example, scan pass, dwell time, and ion dose, to optimize the perovskite etching process and achieved patterned binary and circular MAPbBr₃ subwavelength grating (SWG) reflectors (Figure 11a,b).^[72] Benefiting from the precise etching, the SWG reflector exhibited high reflectivity of above 90% at

a 23 nm-wide spectrum centered at 570 nm. Unfortunately, the surface damage, induced from ion implantation and surface amorphization, and the redeposition of perovskite film in the etching process severely limited its application in optoelectronic and electronic devices. Alias et al. further improved the FIB etching by introducing halide gaseous precursors of XeF₂ and I₂ into the etching process (Figure 11c).^[73] Compared with conventional FIB etching, the gas-assisted FIB demonstrated enhanced etching and controllability, reduced surface damage, and minimized redeposition effect, thus leading seven times enhancement in PL intensity and narrower PL peak (Figure 11d).

ICP etching cooperated with electron-beam lithography (EBL) can also be utilized to achieve nanostructures on bulk materials.^[74] Gao et al. demonstrated a MAPbBr₃ grating with controlled spatial resolution and the highest resolution of 7257 dpi.^[75] Various extrinsic structural colors emitted from the MAPbBr₃ grating of different spatial resolutions, indicating the light–matter interaction (Figure 11e). The etching method is a straightforward patterning strategy performed with the nanoscale resolution, which realized unique optical properties through the light–matter interaction. However, it can introduce inevitable damage to the perovskite film, such as the degradation of the PL intensity after FIB etching.

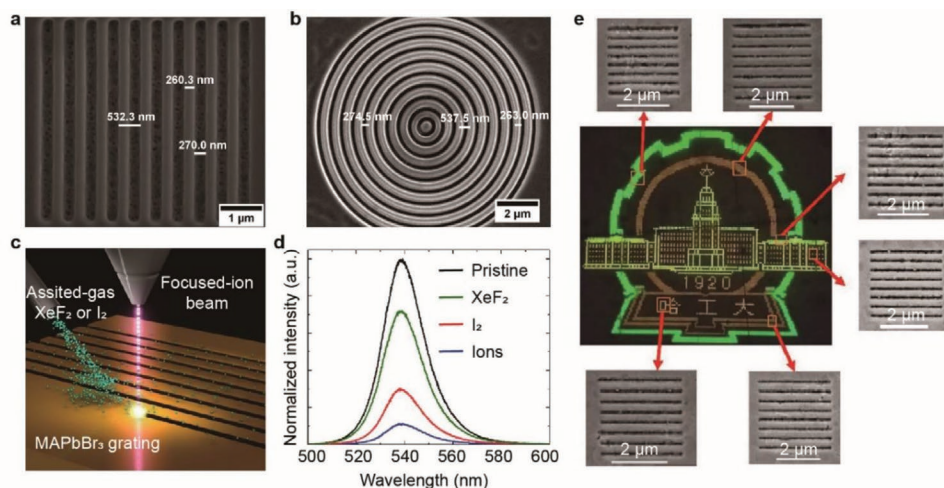


Figure 11. SEM images of a) binary and b) circular MAPbBr₃ subwavelength grating formed by FIB etching. a,b) Reproduced with permission.^[72] Copyright 2015, American Vacuum Society. c) Schematic of injection of XeF₂ and I₂ gas during FIB etching for enhanced etching controllability and marginal surface damage. d) Comparison of PL emission spectra from MAPbBr₃ gratings fabricated via FIB and gas-assisted FIB etching process. c,d) Reproduced with permission.^[73] Copyright 2015, American Chemical Society. e) Optical images of MAPbBr₃ grating with different spatial resolutions under white light illumination. The insets around the logo are the relevant pixel unit SEM image. Reproduced with permission.^[75] Copyright 2018, American Chemical Society.

2.4.3. Inkjet Printing

Inkjet printing technology is another mask-free method to realize perovskite arrays.^[76] Gu et al. fabricated MAPbBr₃ single-crystal microplate arrays on various substrates by inkjet printing (Figure 12a).^[77] Benefiting from the precise and flexible manipulation at the single pixel level, versatile perovskite single crystal arrays were achieved (Figure 12b). Additionally, adhesion force and temperature of the substrate that have great influences on formation of perovskite crystals, were investigated as shown in Figure 12c,d. With the adhesion force decreasing, the morphology of perovskite changed from multiple crystals to single crystal, which may be attributed to the

solid-liquid-gas contact line behavior during solvent evaporation (Figure 12c).^[78] For the substrate with low adhesion, the contact line retracted as the solvent evaporates, resulting in formation of single crystal with regular shape in the center of the droplet. In contrast, long-time pinning of contact line occurred on the high adhesion force substrate during solvent evaporation, leading to multiple crystals distributed around the droplet. Moreover, the single crystal was favorable to be formed at the temperature range of 8–10 °C, which can be explained by the Marangoni convection within the droplet (Figure 12d). By using different inks, a large-scale CsPbBr₃ QD array was also achieved by inkjet printing (Figure 12e,f).^[79] The inhomogeneous distribution was observed on the Au electrodes, which

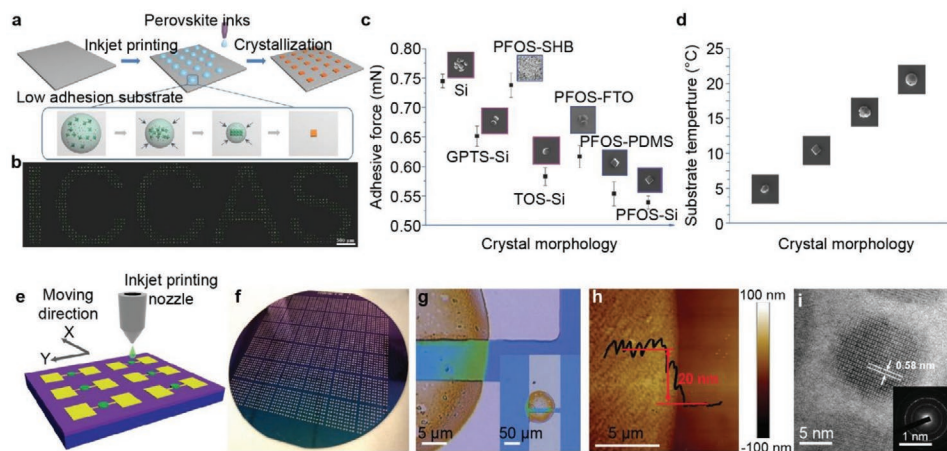


Figure 12. a) Schematic illustration of the fabrication of MAPbBr₃ single crystal microplate arrays by inkjet printing. b) Fluorescence image of large-scale MAPbBr₃ microplate arrays. Crystal morphology of MAPbBr₃ microplates formed on various substrates with c) different adhesive force and d) temperature. a–d) Reproduced with permission.^[77] Copyright 2017, Wiley-VCH. e) Schematic illustration of the fabrication procedures for CsPbBr₃ QDs devices by inkjet printing. f) Photography of CsPbBr₃ QDs based X-ray detector arrays on a 4 in. wafer. g) Optical image and h) height profile of the printed CsPbBr₃ QDs film. i) High-resolution TEM image and SAED pattern of CsPbBr₃ QDs. e–i) Reproduced with permission.^[79] Copyright 2019, Wiley-VCH.

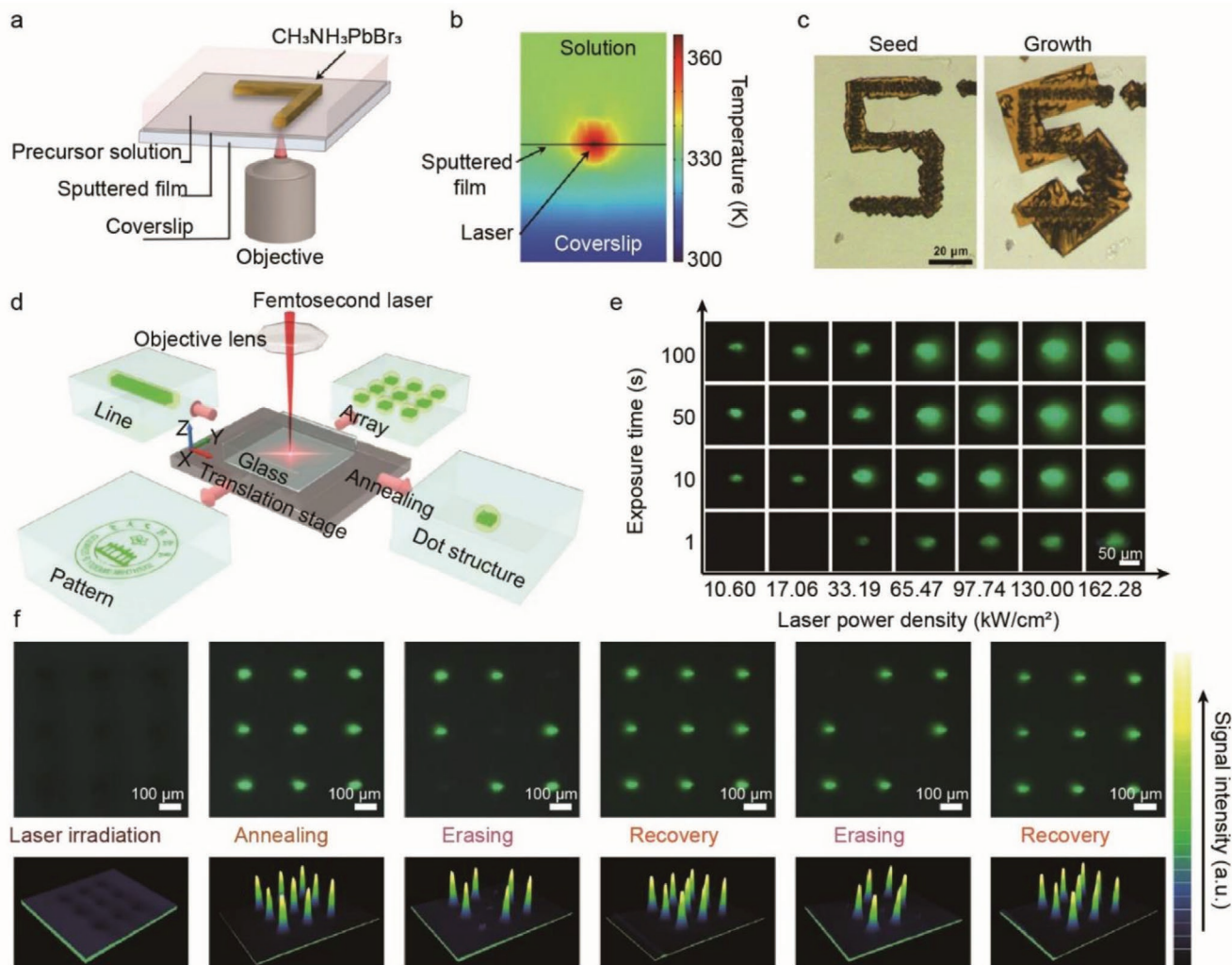


Figure 13. a) Schematic illustration of the laser direct-write method for the MAPbBr₃ patterns. b) Simulation of the temperature gradient at the substrate–solution surface induced by laser. c) Optical images of MAPbBr₃ seed (left panel) and MAPbBr₃ pattern (right panel) after further growth. a–c) Reproduced with permission.^[81] Copyright 2016, American Chemical Society. d) Schematic of the femtosecond laser writing system for CsPbBr₃ QD pattern fabrication. e) Optical images of the CsPbBr₃ QD pattern formed at different laser power densities and exposure times under UV illumination. f) Optical images (upper) and corresponding signal intensities (lower) of the CsPbBr₃ QD pattern during the erasing–recovery cycles under UV illumination. d–f) Reproduced with permission.^[85] Copyright 2019, Nature Publishing Group.

was attributed to the coffee ring effect (Figure 12g). The thickness of the printed dot was around 20 nm with a surface roughness of 4 nm (Figure 12h). As shown in the HRTEM image (Figure 12i), the interplanar distance of the QD was 0.58 nm, which was consistent with the lattice space of (100) plane of the α -phase CsPbBr₃.

2.4.4. Laser-Induced Growth

The perovskite precursors solution (e.g., MABr·PbBr₂ in DMF) presents an inversed relationship between solubility and temperature.^[80] Inspired by this relationship, Chou et al. developed a laser direct-write (LDW) method by utilizing the laser irradiation to generate a temperature gradient to control crystal nuclei sites.^[81] In this approach, Au or C thin film was sputtered on the

coverglass as a light absorber to generate localized heat, thus enabling precise control of perovskite seed growth (Figure 13a). By applying laser irradiation (1 mW) on the target film, an 80 °C temperature rise was generated at the beam-focused position, which is high enough to induce local crystallization (Figure 13b). As moving the beam position, arbitrary shapes of perovskite seed could be formed on the substrate, which was further grown to bulk crystals by pausing the beam movement (Figure 13c). To minimize dissolution, these patterns were synthesized in the near-saturated perovskite precursors solution.

Benefiting from the capability of rapid distribution of atoms, the ultrafast laser, e.g., femtosecond laser, has been applied to construct 3D photonic structures,^[82] to introduce microcracks and to change microarea reflective index.^[83] In addition, it has been proved that the perovskite materials can be morphologically reshaped and decomposed by photon–matter interaction.^[84]

Huang et al. proposed a method of reversible in situ formation and decomposition of CsPbBr₃ QDs through femtosecond laser irradiation.^[85] In this method, the 3D structures comprised of CsPbBr₃ QDs can be formed by femtosecond laser irradiation, decomposed under further laser irradiation and subsequently recovered by low-temperature annealing inside the glass containing Cs, Pb, and Br elements (Figure 13d). The parameters of QDs formation, for example, laser wavelength, power density, exposure time, and annealing temperature, were investigated and optimized. Benefiting from these parameters, the intense green luminescence was observed under UV light indicating the formation of CsPbBr₃ QD circles (Figure 13e). Furthermore, by using a computer-controlled 3D XYZ stage, CsPbBr₃ QD arrays can be formed inside the glass (Figure 13f). The repeating cycle of erasing and recovery processes demonstrated the rewritability of the QD arrays. In addition, benefiting from the protection of the glass matrix, the QD arrays demonstrated much improved long-term stability, which can be stored in water for 30 d with unchanged function and PL properties.

3. Optoelectronic Applications of Perovskite Arrays

The perovskite has led to great success in photovoltaics, which becomes an impetus to exploit various optoelectronic applications, including photodetectors, lasers, LEDs, and nanogratings. The large-scale integrated device arrays offer multidimensional information and many exciting applications in comparison with the traditional single device. Recently, the perovskite-based devices with array configuration have attracted tremendous attention.

3.1. Photodetector Arrays

Photodetection relies on the semiconductor, which is widely used in modern industries such as silicon^[86] or III–V compounds,^[87] that are able to transduce photons to electrical signals for the following processing. Rapid advancing applications, e.g., optical communication, electronic skin, and digital display, create an increasing demand for innovations in photodetectors.^[88] Wu and co-authors reported a 10 × 10 flexible photodetector array with a resolution of 63.5 dpi for photoimaging and real-time light trajectory tracking.^[56] The large-scale patterned CH₃NH₃PbI_{3-x}Cl_x perovskite films were prepared on a polyethylene terephthalate (PET) substrate with periodic hydrophilic–hydrophobic surface functionalization as the photosensing layer. Each pixel consisted of a perovskite film precisely formed on the as-prepared interdigital electrodes and then encapsulated with a thin layer of PDMS to improve device stability (Figure 14a). The photodetector arrays demonstrated satisfactory electric uniformity under both dark and illumination conditions, with the statistical dark current of 1.14 ± 0.64 nA with a 97.5% confidence interval (Figure 14b,c). A customized multi-channel data acquisition system was adopted to characterize the photoimaging performance by converting the photocurrent into voltage changes. As shown in Figure 14d, the moveable light spot was applied on a single pixel through a shadow mask, and

an obvious voltage increasing occurred as the light spot went through corresponding pixel (from pixel no. 1 to 5). Additionally, a designed mask with the letter “H” was utilized to realize the light distribution on the device for photoimaging. The pixels under illumination demonstrated the increase of output voltage while others which were blocked by the mask remained almost unchanged, thus leading to a clear letter “H” from the output voltage (Figure 14e).

The large atomic number of the perovskite constituents, e.g., Pb, Cs, and Sn, combined with high carrier mobility enables the perovskite to be a potential candidate for an X-ray detector.^[89] Liu and co-workers demonstrated a flexible soft X-ray detector array based on CsPbBr₃ QDs through the inkjet printing method (Figure 14f).^[79] Au electrodes were adopted in the detector and output current demonstrated a linear dependence on the applied voltage, indicating Ohmic contact between electrodes and QDs (Figure 14g). As shown in Figure 14h, the device demonstrated good stability with remaining nearly constant under different dose rates, and fast response with the rising time of 30 ms and falling time of 27 ms under 733 mGy_{air} s⁻¹ dose rate. Additively, the output current increased linearly with the dose rates at the range of 0.5–7 mGy_{air} s⁻¹ and the highest sensitivity was calculated to be 1450 μC Gy_{air}⁻¹ cm⁻² with the dose rate of 0.0172 mGy_{air} s⁻¹, which suggested the superior capability of CsPbBr₃ for the conversion of X-ray into electrical signals (Figure 14i).

3.2. LED Arrays

Perovskites possess high color purity, intense photoluminescence, and balanced charge carrier mobility, which make them potential candidates for next-generation LEDs.^[90] Lei and co-workers demonstrated a LED array with the single-crystalline MAPbBr₃ pillar as a single pixel.^[91] The pillar arrays were formed on a bulk MAPbBr₃ crystal through the homoepitaxial growth in the perovskite precursor solution. The crystal position, dimension, morphology, and orientation can be controlled through the open sites and time durations for epitaxial growth (Figure 15a,b). Subsequently, poly(3,4-ethylenedioxythiophene):poly(styrene sulfonate) (PEDOT:PSS) layer which served as the hole-transporting and electron-blocking layer was adopted to build the LED arrays (Figure 15c). The LED arrays can be lighted up at a low voltage of 2–3 V resulting in the uniform and intense light emission from each pixel (Figure 15d). The light intensity increased with drive voltage increasing from 2 V and rapidly saturated at 8 V, which indicates the efficient carrier injection and transport and low leakage current (Figure 15e). A slight decrease of electroluminescence intensity was observed after saturation, which is attributed to the heating effect. The external quantum efficiency (EQE) of the device can reach 6.1% under 9.0 V driving voltage, yielding the internal quantum efficiency of 28.2% at 21.6% top electrode transmission, which was superior to the similar device with polycrystalline perovskites (Figure 15f). Zou and co-workers demonstrated a perovskite LED array for RGB displays based on the dry lift-off approach. The function layers of the LED array consisted of PEDOT:PSS, perovskite, and 2,2',2''-(1,3,5-benzinetriyl)-tris(1-phenyl-1-H-benzimidazole) (TPBi). The SiO₂ insulating layer was adopted to avoid leakage current (Figure 15g). Uniform

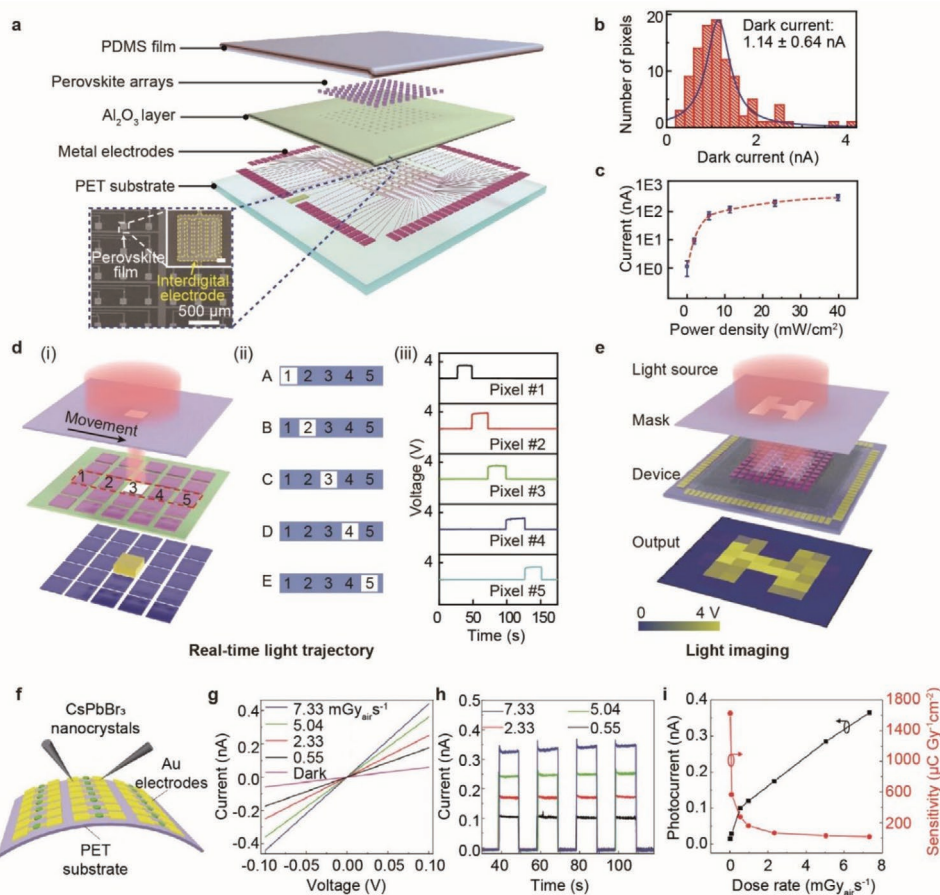


Figure 14. a) Schematic structure of the photodetector arrays. Inset is the SEM image of the array device and a single pixel. b) Statistical dark current of the photodetector arrays. c) Average output current from the photodetector arrays under different illumination intensities. d) Demonstration of real-time light trajectory tracking: i) schematic illustration of the light spot movement and ii) the light trajectory on the device (from pixel no. 1 to pixel no. 5), and iii) the change of output voltage from corresponding pixels while light went through the device. e) The output voltage to image the light distribution. a–e) Reproduced with permission.^[56] Copyright 2018, Wiley-VCH. f) Schematic of an X-ray detector array on PET substrate. g) I – V curves and h) photocurrent response to X-ray from a single pixel under different X-ray dose rates. i) Photocurrents and sensitivity as a function of X-ray dose rate with 0.1 V bias voltage. f–i) Reproduced with permission.^[79] Copyright 2019, Wiley-VCH.

light emission of the LEDs with either square pixels or a complex logo pattern was observed (Figure 15h,i). The light intensity increased with the driven voltage and pure color emission with a narrow line width of 19 nm in the EL spectra was also obtained (Figure 15j). The LED array with 100 square pixels (pixel size: 30 μm) exhibited a typical diode characteristic and its luminance increased sharply after driven voltage exceeding the turn-on voltage (3.4 V) (Figure 15k). After 8.4 V, the decrease of luminance occurred due to the Joule heat and Auger recombination. Compared with the nonpatterned LEDs, the LED array demonstrated deteriorated performance in EQE, which was attributed to the large leakage current caused by a few bad pixels and imperfect pixel edges (Figure 15l).

3.3. Laser Arrays: Fabry–Perot (FP) and Whispering Gallery Mode (WGM)

Perovskite NWs have demonstrated satisfactory lasing performance due to the superior optoelectronic properties.^[92] Each

perovskite NW with smooth surface could serve as a waveguide along its axial direction and two parallel end facets of the NW form a FP cavity.^[7a] Liu and co-workers reported a perovskite NW laser array with identical optical mode (Figure 16a).^[27] Under optical excitation, these MAPbBr₃ NWs lased at room temperature with a set of peaks at ≈ 543 nm emitted mostly come from the two end facets (Figure 16b). The s-curve for laser oscillation is observed in Figure 16c. It indicates that the spontaneous emission transition to amplified spontaneous emission at thresholds of 12.3 $\mu\text{J cm}^{-2}$, and further laser oscillation occurred at 18.3 $\mu\text{J cm}^{-2}$. The effect of NW length on the cavity was investigated (Figure 16d). It demonstrated a clear linear relationship between the mode spacing and $1/\text{length}$, which confirmed an FP microcavity formed along the length.

WGM resonant cavity can also be built inside the perovskite wires. Yang et al. demonstrated a single-mode WGM laser array based on the CsPbBr₃ MWs.^[31] As shown in Figure 16e, with increasing the optical excitation up to the thresholds, the transition from spontaneous emission to stimulated emission occurred, leading to a single sharp peak

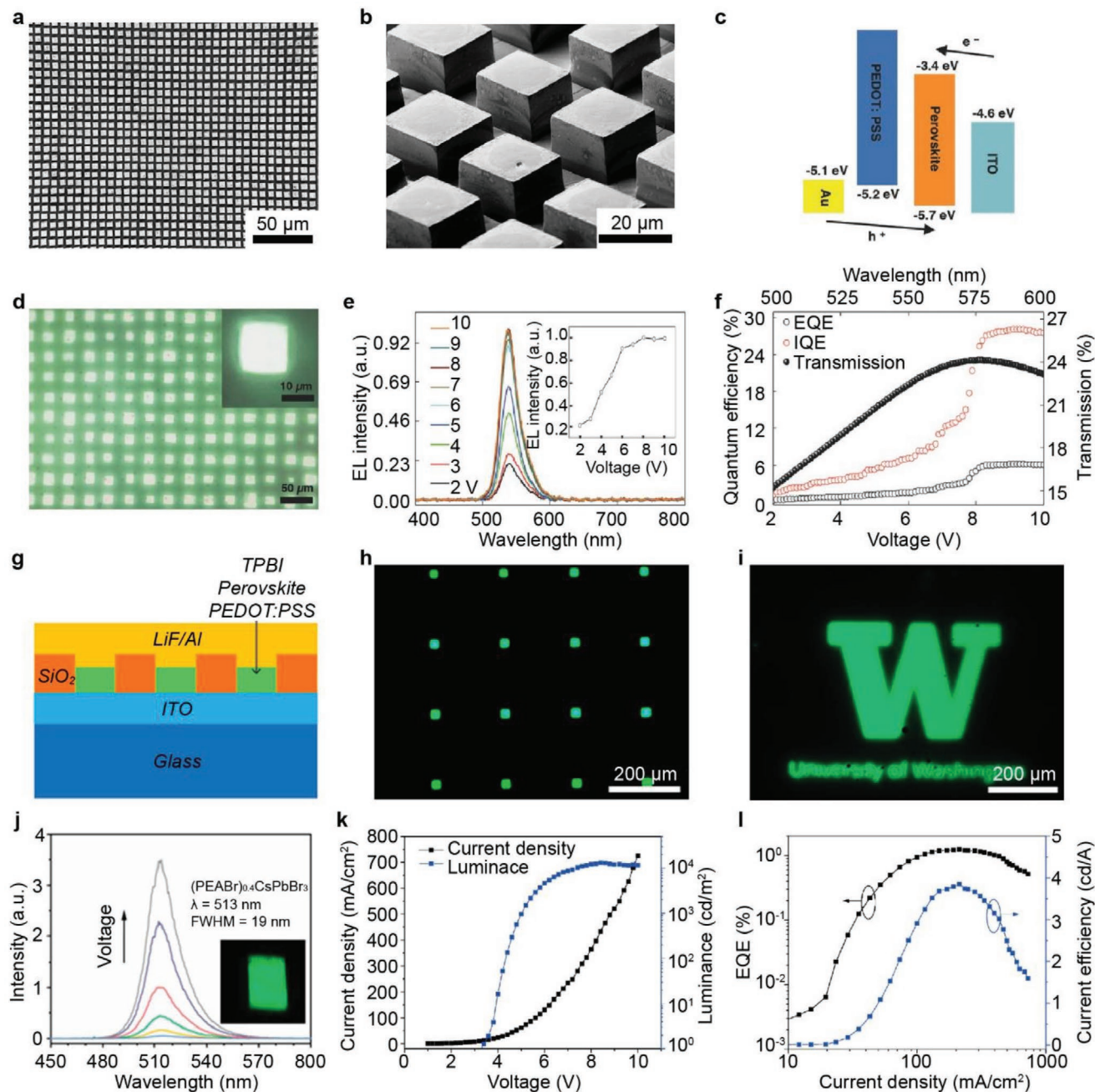


Figure 15. a) Top view and b) tilted view SEM images of an epitaxial MAPbBr₃ crystal array. c) Band energy diagram of the LEDs. d) Optical image of a working LED array and an enlarged view of a single pixel (inset). e) Normalized EL intensity at different driven voltage, which saturates at around 8 V (inset). f) Quantum efficiency and transmission of the LED array. a–f) Reproduced with permission.^[91] Copyright 2018, Wiley-VCH. g) Schematic illustration of the structure of the LED array. Optical image of a working LED array: h) 30 μm square pixel, and i) University of Washington logo. j) Normalized EL intensity at different driven voltages from 3 to 5 V. The inset is a photograph of a working LED (2 × 2 mm²). k) Dependence of current density and luminance on the driven voltage. l) Dependence of EQE and current efficiency on the current density. g–l) Reproduced with permission.^[53] Copyright 2020, American Chemical Society.

that grew rapidly with further pump density increasing. By plotting the PL intensity as a function of pump density, an inflection point, which is the threshold, was obtained in this process, and full-width at half-maximum (FWHM) experienced a sharp decrease after this point (Figure 16f). It is worth noting that no other lasing peaks appeared with

increasing pump density while a blueshift less than 1 nm happened due to the band filling effect, which confirmed the single-mode lasing behavior. The laser peak was well fitted with a Lorentzian function with the FWHM of 0.35 nm and Q factor of ≈1555 (Figure 16g). Additionally, the free spectral range presents a linear relationship with the MW length,

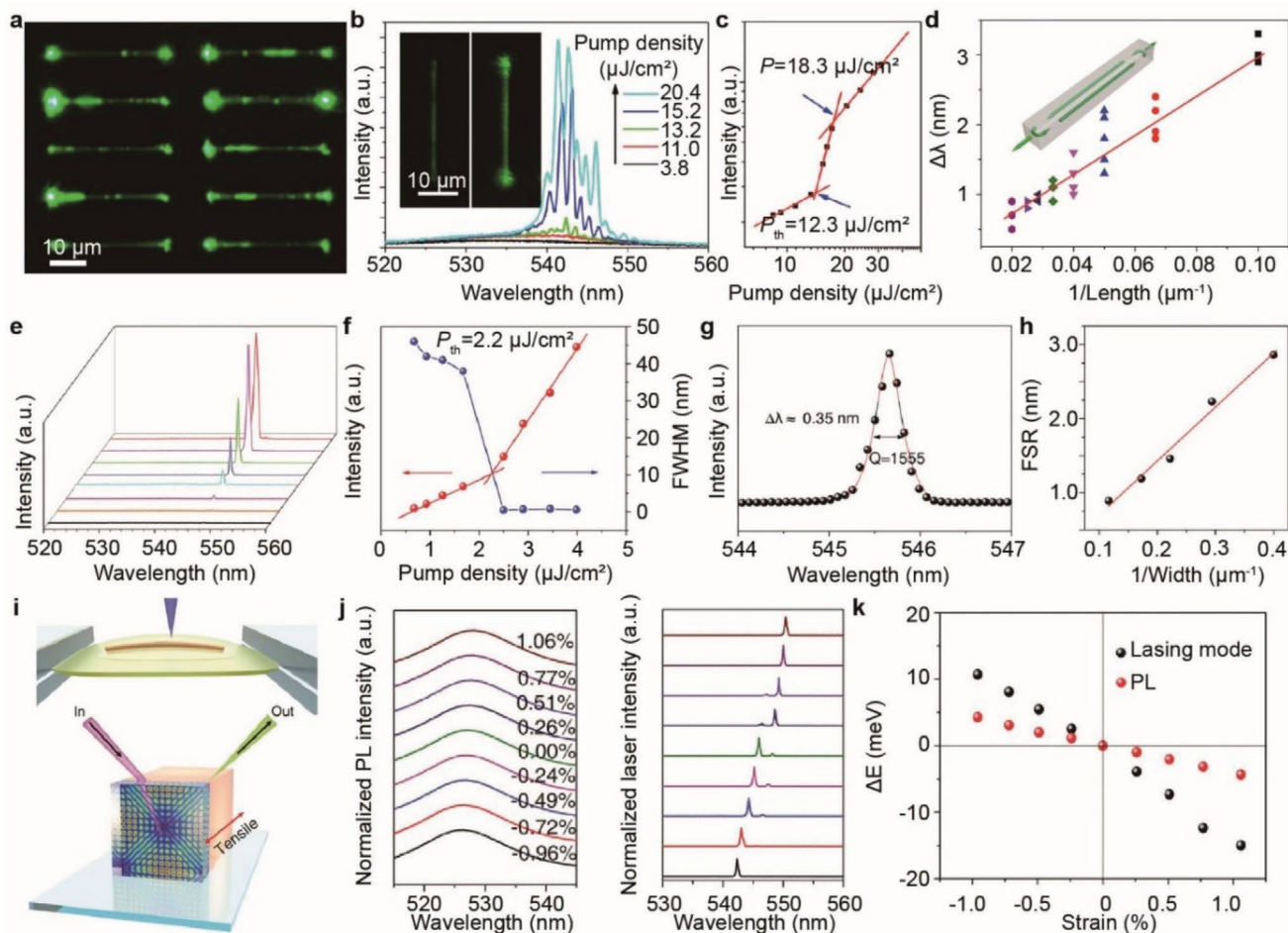


Figure 16. a) Fluorescence image of a MAPbBr₃ NW array above the laser threshold. b) PL spectrum of a single NW at different pump densities. Insets are the corresponding fluorescence images below (left) and above (right) the laser threshold. c) Integrated PL intensity as a function of pump density. d) Mode spacing $\Delta\lambda$ around $\lambda = 543$ nm as a function of $1/\text{length}$ of NW. a–d) Reproduced with permission.^[27] Copyright 2017, American Chemical Society. e) PL spectrum of a single CsPbBr₃ microwire at different pump densities. f) Integrated PL intensity and FWHM as a function of pump density. g) Lorentzian fitting of a lasing peak, showing the Q factor of 1555 and the FWHM of 0.35 nm. h) FSR as a function of $1/\text{length}$ of CsPbBr₃ microwire. i) Schematic of a CsPbBr₃ microwire under tensile strain. j) Stimulated PL spectrum and spontaneous emission from a CsPbBr₃ microwire under different strain states. k) The blue/redshift of a CsPbBr₃ microwire at PL and lasing mode under different strain states. e–k) Reproduced with permission.^[31] Copyright 2019, Wiley-VCH.

which coincides with the laser behavior from a square WGM cavity (Figure 16h).

Moreover, the CsPbBr₃ materials possess intrinsic piezoelectric and ferroelectric properties, which can modulate crucial lasing parameters, e.g., bandgap and refractive index.^[93] Consequently, the MWs were transferred onto a flexible PET substrate to analyze the strain effect on the microcavity (Figure 16i). Both the PL emission and lasing mode demonstrated a similar trend that a redshift occurred with tensile strain while the blueshift was caused by compressive strain (Figure 16j). However, the slopes of these shifts with strains in PL and lasing mode were different, indicating various underlying mechanisms (Figure 16k). The shift of PL emission was attributed to the bandgap changing induced by lattice deformation while the refractive index changing was induced by piezoelectric polarization effect resulting in the lasing movement.

3.4. Nanogratings

Nanostructured semiconductors exhibit unique optical properties, such as enhanced absorption,^[94] broadband light emitting,^[95] and increased binding energy.^[96] Alias et al. demonstrated a SWG of MAPbBr₃ with broadband absorption through the gas-assisted FIB etching method.^[73] Benefitting from optimized parameters of the period, thickness and fill factor, the SWG absorber realized high absorption of >90% at a broadband spectrum of 500–1000 nm for both transverse electric (TE) and transverse magnetic (TM) polarization (Figure 17a). The computed TE and TM electric field distributions confirmed the high absorption (Figure 17b,c). The incident light was trapped between the grating and air interface without light distribution in air media, which indicates that light was absorbed by the gratings for both polarization. Additionally, the perovskite materials can provide two types of colors that are extrinsic structural

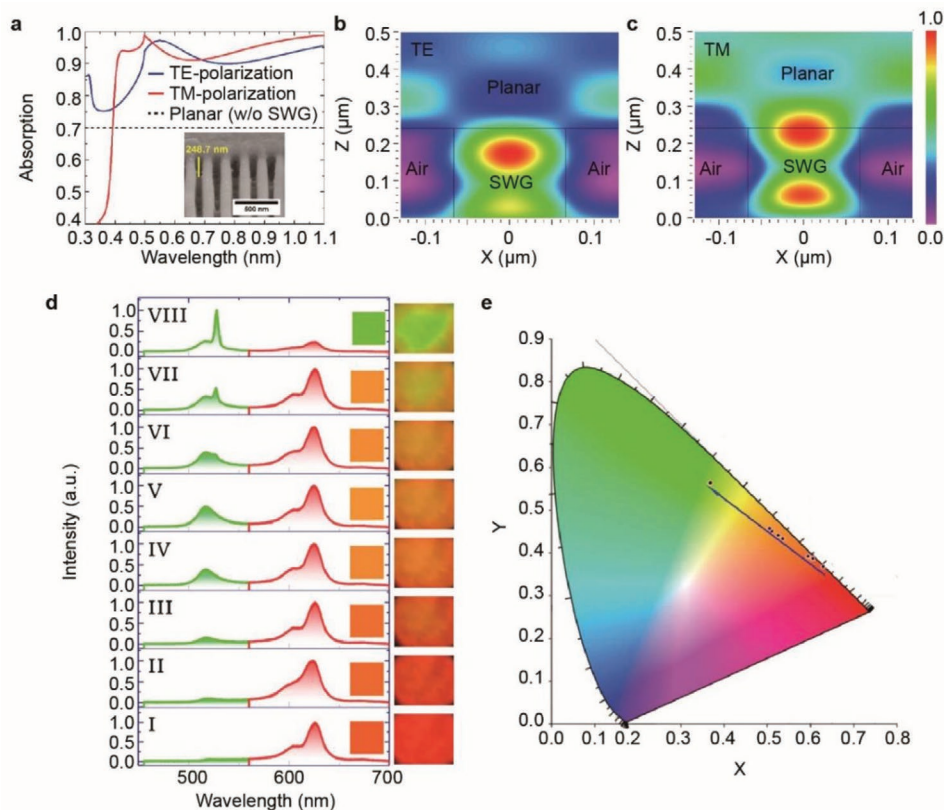


Figure 17. a) Absorption of a MAPbBr₃ subwavelength grating on the broadband spectrum for both TE and TM polarizations. b,c) Electric field distribution of TE and TM polarizations from a period of gratings. a–c) Reproduced with permission.^[73] Copyright 2015, American Chemical Society. d) Recorded spectrum and corresponding colors of MAPbBr₃ gratings under the illumination of white light and Ti:sapphire laser. e) Plot of corresponding colors from (d) in the CIE 1931 color map. d,e) Reproduced with permission.^[75] Copyright 2018, American Chemical Society.

color, tuned by the grating period, and intrinsic emission color, controlled by external pumping density.^[97] By mixing these two types of colors, Gao et al. proposed a concept of in situ dynamic color display, which consisted of a MAPbBr₃ grating with a certain period and the color was tuned by excitation density.^[75] Under only white light illumination, a red reflection color is extrinsic structural color, centered at ≈ 625 nm was observed in the panel I of Figure 17d. Subsequently, when the grating was illuminated with laser simultaneously, an additional green color, intrinsic emission color, centered at 515 nm appeared, leading to a mixed color emission. The brightness of green color increased with pumping density while the reflection red color was suppressed, thus enabling display color to dynamically transit from red to orange and finally to green (Figure 17d). The corresponding color was plotted in the CIE 1931 color map to demonstrate the display color transition path (Figure 17e). Moreover, the suppressed red color can recover to the original level by decreasing the laser intensity to realize reversible color tuning. The color gamut can also be enriched by varying the grating period and changing the stoichiometry of MAPbX₃.

4. Conclusions and Outlook

Metal halide perovskite arrays have attracted widespread attention as a promising component for integrated optoelectronics,

due to their superior optoelectronic properties, facile low-temperature fabrication, and compatibility with the flexible substrate. Here, we reviewed the state-of-the-art perovskite material arrays with the construction methods for single/polycrystalline wires or films, including template-assisted growth, substrate-assisted growth, capillary force-assisted growth, and direct patterning technologies, and their applications in various integrated optoelectronic devices.

In general, the abovementioned construction methods are universal for various perovskite arrays. By using different precursor combinations, various perovskites can be synthesized through similar method, such as that both MAPbBr₃ microplates and layered perovskite ((BA)₂(MA)_{n-1}Pb_nI_{3n+1}) NWs can be synthesized through capillary bridge lithography method; MAPbI₃, CsPbBr₃, and lead-free perovskite (MASnI₃) NW arrays were demonstrated via AAO template-assisted growth method. Considering the specific requirements on the material properties and the compatibility with subsequent application, there is optimal construction method of the perovskite array for each device. For example, the polarization-sensitive photodetector was realized by NW arrays through capillary trailing lithography, while WGM mode laser array was fabricated through the PDMS template with square grooves.

Although the construction method of the perovskite arrays has experienced rapid development, many challenges remain regarding the large-scale integration and practical applications.

- i) Compared with the polycrystalline thin film, single-crystal perovskite is free of grain boundaries and demonstrates minimized charge trap state density and enhanced carrier mobility, which is the optimal choice for array configurations. Currently, most of the single-crystal perovskite arrays are realized through the solution-processed template-assisted growth, which lacks in precise control on the pixel position and dimensions. The fabrication of large-scale, high-resolution single-crystal perovskite arrays with desired morphology and dimension is still a challenge, especially considering the compatibility with flexible substrate.
- ii) The uniformity and reproducibility of perovskite arrays need to be improved for the integrated optoelectronics. The material properties of each pixel such as the trap state density and mobility demonstrate wide variation from different batches. It may be attributed to the uncontrollable nucleation during the rapid reaction of the two precursors. Compared with mixing the precursors for one-step crystallization, the seed deposition followed by crystal epitaxial growth can effectively control the nuclei sites and suppress the random nucleation process to improve the array uniformity and reproducibility, which will attract more attention in the future research.
- iii) The family of perovskite in the array configuration will continue to expand. Compositional engineering, by substituting lead with nontoxic metal ions, will result in more environmentally friendly materials with novel properties. In addition, specific growth methods should be applied to various perovskite systems, such as 2D layered perovskites with improved stability and optoelectronic properties. Considering the structural diversity, there is a large scope for the construction of novel perovskite arrays.
- iv) The long-term stability of perovskite arrays needs to be improved in optoelectronic devices. Encapsulation is a cost-effective strategy to improve stability. The encapsulation layer should protect the perovskite array from moisture corrosion and oxygen penetration as well as avoid thermal accumulation. However, the encapsulation layer usually largely increases the thickness of devices up to tens or hundreds of micrometers. It will, therefore, be of urgent need to develop the ultrathin encapsulation for enhanced stability and paving the way for flexible perovskite devices.
- v) The integrated perovskite devices array should provide the working mode that can operate electrically/optically on a single or a few devices in the array. That requires an excellent alignment between perovskite arrays and separated electrodes or patterned samples. Perovskite photodetector arrays and LED arrays have demonstrated these functions through employing separated electrodes; however, the pixel-addressable laser arrays are still absent. Modified photolithography combined with the optimized crystallization process, enabling precise control of the position, resolution, dimension, and morphology of each pixels as well as facilitating the alignment, will be a promising method to achieve the high-resolution and pixel-addressable integrated array devices. Novel device structures employing advanced technologies such as multiplexing are expected for data collection and transmission in high-resolution device arrays.

In short, an ideal and common array construction method should be performed at low-temperature condition on the rigid or flexible substrate, be compatible with conventional photolithography to enable high-resolution and precise control on pixels, possess good reproducibility, and be facile for the fabrication of large-scale array devices. With much achieved encouraging processes in perovskite arrays, we expect the perovskite arrays could potentially revolutionize technological applications, and promote the development of such integrated optoelectronic and photonic devices.

Acknowledgements

X.H. and W.W. contributed equally to this work. The authors thank the support of national key R&D project from Minister of Science and Technology, China (2016YFA0202703), National Natural Science Foundation of China (Nos. 61675027, 51622205, 51432005, 61805015, and 61804011), Beijing City Committee of Science and Technology (Z171100002017019 and Z181100004418004), Beijing Natural Science Foundation (4181004, 4182080, 4184110, 2184131, and Z180011), and Shenzhen Science and Technology Program (Grant No. KQTD20170810105439418).

Conflict of Interest

The authors declare no conflict of interest.

Keywords

array configurations, array construction methods, integrated devices, metal halide perovskite, optoelectronic applications

Received: June 21, 2020

Revised: August 27, 2020

Published online:

- [1] Z. W. Xiao, Y. F. Yan, *Adv. Energy Mater.* **2017**, *7*, 1701136.
- [2] a) G. C. Xing, N. Mathews, S. Y. Sun, S. S. Lim, Y. M. Lam, M. Gratzel, S. Mhaisalkar, T. C. Sum, *Science* **2013**, *342*, 344; b) E. Edri, S. Kirmayer, S. Mukhopadhyay, K. Gartsman, G. Hodes, D. Cahen, *Nat. Commun.* **2014**, *5*, 3461; c) Q. F. Dong, Y. J. Fang, Y. C. Shao, P. Mulligan, J. Qiu, L. Cao, J. S. Huang, *Science* **2015**, *347*, 967.
- [3] a) D. Shi, V. Adinolfi, R. Comin, M. J. Yuan, E. Alarousu, A. Buin, Y. Chen, S. Hoogland, A. Rothenberger, K. Katsiev, Y. Losovyj, X. Zhang, P. A. Dowben, O. F. Mohammed, E. H. Sargent, O. M. Bakr, *Science* **2015**, *347*, 519; b) M. I. Saidaminov, V. Adinolfi, R. Comin, A. L. Abdelhady, W. Peng, I. Dursun, M. Yuan, S. Hoogland, E. H. Sargent, O. M. Bakr, *Nat. Commun.* **2015**, *6*, 8724; c) Y. C. Liu, J. K. Sun, Z. Yang, D. Yang, X. D. Ren, H. Xu, Z. P. Yang, S. Z. Liu, *Adv. Opt. Mater.* **2016**, *4*, 1829.
- [4] a) Y. Q. Xu, Q. Chen, C. F. Zhang, R. Wang, H. Wu, X. Y. Zhang, G. C. Xing, W. W. Yu, X. Y. Wang, Y. Zhang, M. Xiao, *J. Am. Chem. Soc.* **2016**, *138*, 3761; b) F. Deschler, M. Price, S. Pathak, L. E. Klintberg, D. D. Jarausch, R. Higler, S. Hüttner, T. Leijtens, S. D. Stranks, H. J. Snaith, M. Atature, R. T. Phillips, R. H. Friend, *J. Phys. Chem.* **2014**, *5*, 1421; c) S. Adjokatse, H. H. Fang, M. A. Loi, *Mater. Today* **2017**, *20*, 413.
- [5] a) M. M. Lee, J. Teuscher, T. Miyasaka, T. N. Murakami, H. J. Snaith, *Science* **2012**, *338*, 643; b) N. J. Jeon, H. G. Lee, Y. C. Kim, J. Seo,

- J. H. Noh, J. Lee, S. I. Seok, *J. Am. Chem. Soc.* **2014**, *136*, 7837; c) N. G. Park, *Mater. Today* **2015**, *18*, 65; d) G. P. Mao, W. Wang, S. Shao, X. J. Sun, S. A. Chen, M. H. Li, H. M. Li, *Rare Met.* **2018**, *37*, 95; e) J. L. Sun, Q. L. Hua, R. R. Zhou, D. M. Li, W. X. Guo, X. Y. Li, G. F. Hu, C. X. Shan, Q. B. Meng, L. Dong, C. F. Pan, Z. L. Wang, *ACS Nano* **2019**, *13*, 4507.
- [6] a) L. T. Dou, Y. Yang, J. B. You, Z. R. Hong, W. H. Chang, G. Li, Y. Yang, *Nat. Commun.* **2014**, *5*, 5404; b) Y. Lee, J. Kwon, E. Hwang, C. H. Ra, W. J. Yoo, J. H. Ahn, J. H. Park, J. H. Cho, *Adv. Mater.* **2015**, *27*, 41; c) D. Hao, J. Zou, J. Huang, *InfoMat* **2020**, *2*, 139.
- [7] a) H. M. Zhu, Y. P. Fu, F. Meng, X. X. Wu, Z. Z. Gong, Q. Ding, M. V. Gustafsson, M. T. Trinh, S. Jin, X. Y. Zhu, *Nat. Mater.* **2015**, *14*, 636; b) S. A. Veldhuis, P. P. Boix, N. Yantara, M. J. Li, T. C. Sum, N. Mathews, S. G. Mhaisalkar, *Adv. Mater.* **2016**, *28*, 6804; c) J. Chen, W. Du, J. Shi, M. Li, Y. Wang, Q. Zhang, X. Liu, *InfoMat* **2020**, *2*, 170.
- [8] a) Z. K. Tan, R. S. Moghaddam, M. L. Lai, P. Docampo, R. Higler, F. Deschler, M. Price, A. Sadhanala, L. M. Pazos, D. Credgington, F. Hanusch, T. Bein, H. J. Snaith, R. H. Friend, *Nat. Nanotechnol.* **2014**, *9*, 687; b) Z. G. Xiao, R. A. Kerner, L. F. Zhao, N. L. Tran, K. M. Lee, T. W. Koh, G. D. Scholes, B. P. Rand, *Nat. Photonics* **2017**, *11*, 108; c) B. R. Sutherland, E. H. Sargent, *Nat. Photonics* **2016**, *10*, 295; d) Y. Liu, L. K. Ono, Y. Qi, *InfoMat* **2020**, <https://doi.org/10.1002/inf2.12098>.
- [9] A. Kojima, K. Teshima, Y. Shirai, T. Miyasaka, *J. Am. Chem. Soc.* **2009**, *131*, 6050.
- [10] Best Research-Cell Efficiency Chart NREL, <https://www.nrel.gov/pv/cell-efficiency.html> (Accessed: January 2020).
- [11] H. C. Cho, S. H. Jeong, M. H. Park, Y. H. Kim, C. Wolf, C. L. Lee, J. H. Heo, A. Sadhanala, N. Myoung, S. Yoo, S. H. Im, R. H. Friend, T. W. Lee, *Science* **2015**, *350*, 1222.
- [12] a) K. B. Lin, J. Xing, L. N. Quan, F. P. G. de Arquer, X. W. Gong, J. X. Lu, L. Q. Xie, W. J. Zhao, D. Zhang, C. Z. Yan, W. Q. Li, X. Y. Liu, Y. Lu, J. Kirman, E. H. Sargent, Q. H. Xiong, Z. H. Wei, *Nature* **2018**, *562*, 245; b) Y. Cao, N. N. Wang, H. Tian, J. S. Guo, Y. Q. Wei, H. Chen, Y. F. Miao, W. Zou, K. Pan, Y. R. He, H. Cao, Y. Ke, M. M. Xu, Y. Wang, M. Yang, K. Du, Z. W. Fu, D. C. Kong, D. X. Dai, Y. Z. Jin, G. Q. Li, H. Li, Q. M. Peng, J. P. Wang, W. Huang, *Nature* **2018**, *562*, 249.
- [13] L. N. Quan, B. P. Rand, R. H. Friend, S. G. Mhaisalkar, T. W. Lee, E. H. Sargent, *Chem. Rev.* **2019**, *119*, 7444.
- [14] a) M. Hu, C. Bi, Y. Yuan, Y. Bai, J. Huang, *Adv. Sci.* **2016**, *3*, 1500301; b) X. Ren, Z. Yang, D. Yang, X. Zhang, D. Cui, Y. Liu, Q. Wei, H. Fan, S. F. Liu, *Nanoscale* **2016**, *8*, 3816.
- [15] a) K. S. Novoselov, A. Mishchenko, A. Carvalho, A. H. C. Neto, *Science* **2016**, *353*, aac9439; b) Z. Yang, Y. Deng, X. Zhang, S. Wang, H. Chen, S. Yang, J. Khurgin, N. X. Fang, X. Zhang, R. Ma, *Adv. Mater.* **2018**, *30*, 1704333; c) Z. Yang, Q. Xu, X. Wang, J. Lu, H. Wang, F. Li, L. Zhang, G. Hu, C. Pan, *Adv. Mater.* **2018**, *30*, 1802110.
- [16] a) J. Feng, B. Xiao, *J. Phys. Chem. C* **2014**, *118*, 19655; b) B. Saparov, J.-P. Sun, W. Meng, Z. Xiao, H.-S. Duan, O. Gunawan, D. Shin, I. G. Hill, Y. Yan, D. B. Mitzi, *Chem. Mater.* **2016**, *28*, 2315; c) S. Shao, J. Liu, G. Portale, H. H. Fang, G. R. Blake, G. H. ten Brink, L. J. A. Koster, M. A. Loi, *Adv. Energy Mater.* **2018**, *8*, 1702019; d) F. Cao, W. Tian, M. Wang, M. Wang, L. Li, *InfoMat* **2020**, *2*, 577.
- [17] a) D. J. Sirbuly, G. M. Lowman, B. Scott, G. D. Stucky, S. K. Buratto, *Adv. Mater.* **2003**, *15*, 149; b) D.-Y. Khang, H. Jiang, Y. Huang, J. A. Rogers, *Science* **2006**, *311*, 208; c) S. Fang, H. Wang, J. Y. Yang, S. G. Lu, B. Yu, J. T. Wang, C. R. Zhao, *Rare Met.* **2019**, *38*, 776.
- [18] a) S. Huang, L. Dai, A. W. Mau, *Adv. Mater.* **2002**, *14*, 1140; b) L. Xiang, H. Zhang, G. Dong, D. Zhong, J. Han, X. Liang, Z. Zhang, L.-M. Peng, Y. Hu, *Nat. Electron.* **2018**, *1*, 237.
- [19] a) J. Yun, Y. Lim, G. N. Jang, D. Kim, S. J. Lee, H. Park, S. Y. Hong, G. Lee, G. Zi, J. S. Ha, *Nano Energy* **2016**, *19*, 401; b) J. M. Pomirol, P. Q. Liu, T. M. Slipchenko, A. Y. Nikitin, L. Martin-Moreno, J. Faist, A. B. Kuzmenko, *Nat. Commun.* **2017**, *8*, 14626; c) J. Ren, W. Zhang, Y. Wang, Y. Wang, J. Zhou, L. Dai, M. Xu, *InfoMat* **2019**, *1*, 396.
- [20] a) X. Han, W. Du, R. Yu, C. Pan, Z. L. Wang, *Adv. Mater.* **2015**, *27*, 7963; b) C. Pan, L. Dong, G. Zhu, S. Niu, R. Yu, Q. Yang, Y. Liu, Z. L. Wang, *Nat. Photonics* **2013**, *7*, 752; c) R. Li, P. Dapkus, M. E. Thompson, W. Jeong, C. Harrison, P. Chaikin, R. A. Register, D. Adamson, *Appl. Phys. Lett.* **2000**, *76*, 1689; d) T. S. Kim, S.-M. Kim, Y. H. Jang, G. Y. Jung, *Appl. Phys. Lett.* **2007**, *91*, 171114; e) J. H. Yang, J. F. Gao, S. L. Yong, X. L. Ma, L. J. Liu, *Rare Met.* **2019**, *38*, 1097; f) Y. Y. Peng, J. F. Lu, D. F. Peng, W. D. Ma, F. T. Li, Q. S. Chen, X. D. Wang, J. L. Sun, H. T. Liu, C. F. Pan, *Adv. Funct. Mater.* **2019**, *29*, 1905051; g) R. R. Bao, C. F. Wang, L. Dong, R. M. Yu, K. Zhao, Z. L. Wang, C. F. Pan, *Adv. Funct. Mater.* **2015**, *25*, 2884; h) P. Lin, C. Pan, Z. L. Wang, *Mater. Today Nano* **2018**, *4*, 17.
- [21] a) Y. Fu, H. Zhu, J. Chen, M. P. Hautzinger, X.-Y. Zhu, S. Jin, *Nat. Rev. Mater.* **2019**, *4*, 169; b) Z. Cheng, J. Lin, *CrystEngComm* **2010**, *12*, 2646.
- [22] J. M. Ball, A. Petrozza, *Nat. Energy* **2016**, *1*, 16149.
- [23] a) E. J. Juarez-Perez, Z. Hawash, S. R. Raga, L. K. Ono, Y. B. Qi, *Energy Environ. Sci.* **2016**, *9*, 3406; b) J. A. Christians, P. A. M. Herrera, P. V. Kamat, *J. Am. Chem. Soc.* **2015**, *137*, 1530; c) S. H. Wang, Y. Jiang, E. J. Juarez-Perez, L. K. Ono, Y. B. Qi, *Nat. Energy* **2017**, *2*, 16195.
- [24] C. Kagan, T. Breen, L. Kosbar, *Appl. Phys. Lett.* **2001**, *79*, 3536.
- [25] Z. Cheng, Z. Wang, R. Xing, Y. Han, J. Lin, *Chem. Phys. Lett.* **2003**, *376*, 481.
- [26] a) A. Kim, K. S. Jang, J. Kim, J. C. Won, M. H. Yi, H. Kim, D. K. Yoon, T. J. Shin, M. H. Lee, J. W. Ka, *Adv. Mater.* **2013**, *25*, 6219; b) Z. Zhang, Z. Wang, Z. Xu, Q. Gao, P. Liu, J. Ren, M. Li, C. Zhou, Q. Liao, H. Fu, *Adv. Opt. Mater.* **2018**, *6*, 1800219.
- [27] P. Liu, X. He, J. Ren, Q. Liao, J. Yao, H. Fu, *ACS Nano* **2017**, *11*, 5766.
- [28] X. He, P. Liu, H. Zhang, Q. Liao, J. Yao, H. Fu, *Adv. Mater.* **2017**, *29*, 1604510.
- [29] H. Zhang, Q. Liao, Y. Wu, Z. Zhang, Q. Gao, P. Liu, M. Li, J. Yao, H. Fu, *Adv. Mater.* **2018**, *30*, 1706186.
- [30] a) Y. Wang, J. Wu, P. Zhang, D. Liu, T. Zhang, L. Ji, X. Gu, Z. D. Chen, S. Li, *Nano Energy* **2017**, *39*, 616; b) S. Paek, P. Schouwink, E. N. Athanasopoulou, K. Cho, G. Grancini, Y. Lee, Y. Zhang, F. Stellacci, M. K. Nazeeruddin, P. Gao, *Chem. Mater.* **2017**, *29*, 3490.
- [31] Z. Yang, J. Lu, M. Zhuge, Y. Cheng, J. Hu, F. Li, S. Qiao, Y. Zhang, G. Hu, Q. Yang, *Adv. Mater.* **2019**, *31*, 1900647.
- [32] a) D. Xu, Y. Xu, D. Chen, G. Guo, L. Gui, Y. Tang, *Adv. Mater.* **2000**, *12*, 520; b) M. Schierhorn, S. W. Boettcher, S. Kraemer, G. D. Stucky, M. Moskovits, *Nano Lett.* **2009**, *9*, 3262.
- [33] K. Kim, M. Kim, S. M. Cho, *Mater. Chem. Phys.* **2006**, *96*, 278.
- [34] J. Duay, E. Gillette, R. Liu, S. B. Lee, *Phys. Chem. Chem. Phys.* **2012**, *14*, 3329.
- [35] M. J. Ashley, M. N. O'Brien, K. R. Hedderick, J. A. Mason, M. B. Ross, C. A. Mirkin, *J. Am. Chem. Soc.* **2016**, *138*, 10096.
- [36] A. Waleed, M. M. Tavakoli, L. Gu, Z. Wang, D. Zhang, A. Manikandan, Q. Zhang, R. Zhang, Y. Chueh, Z. Fan, *Nano Lett.* **2017**, *17*, 523.
- [37] L. Gu, M. M. Tavakoli, D. Zhang, Q. Zhang, A. Waleed, Y. Xiao, K. H. Tsui, Y. Lin, L. Liao, J. Wang, *Adv. Mater.* **2016**, *28*, 9713.
- [38] M. M. Tavakoli, A. Waleed, L. Gu, D. Zhang, R. Tavakoli, B. Lei, W. Su, F. Fang, Z. Fan, *Nanoscale* **2017**, *9*, 5828.
- [39] A. Waleed, M. M. Tavakoli, L. Gu, S. Hussain, D. Zhang, S. Poddar, Z. Wang, R. Zhang, Z. Fan, *Nano Lett.* **2017**, *17*, 4951.
- [40] H. C. Kwon, A. Kim, H. Lee, D. Lee, S. Jeong, J. Moon, *Adv. Energy Mater.* **2016**, *6*, 1601055.
- [41] Y. C. Zheng, S. Yang, X. Chen, Y. Chen, Y. Hou, H. G. Yang, *Chem. Mater.* **2015**, *27*, 5116.

- [42] W. Nie, H. Tsai, R. Asadpour, J.-C. Blancon, A. J. Neukirch, G. Gupta, J. J. Crochet, M. Chhowalla, S. Tretiak, M. A. Alam, *Science* **2015**, *347*, 522.
- [43] B. Leung, J. Song, Y. Zhang, J. Han, *Adv. Mater.* **2013**, *25*, 1285.
- [44] L. Lee, J. Baek, K. S. Park, Y.-E. Lee, N. K. Shrestha, M. M. Sung, *Nat. Commun.* **2017**, *8*, 15882.
- [45] a) S. W. Eaton, M. Lai, N. A. Gibson, A. B. Wong, L. Dou, J. Ma, L.-W. Wang, S. R. Leone, P. Yang, *Proc. Natl. Acad. Sci. USA* **2016**, *113*, 1993; b) Y. Tong, B. J. Bohn, E. Bladt, K. Wang, P. Müller-Buschbaum, S. Bals, A. S. Urban, L. Polavarapu, J. Feldmann, *Angew. Chem., Int. Ed.* **2017**, *56*, 13887.
- [46] W. Deng, X. Zhang, L. Huang, X. Xu, L. Wang, J. Wang, Q. Shang, S. T. Lee, J. Jie, *Adv. Mater.* **2016**, *28*, 2201.
- [47] a) X. D. Wang, H. L. Zhang, R. M. Yu, L. Dong, D. F. Peng, A. H. Zhang, Y. Zhang, H. Liu, C. F. Pan, Z. L. Wang, *Adv. Mater.* **2015**, *27*, 2324; b) R. R. Bao, C. F. Wang, Z. C. Peng, C. Ma, L. Dong, C. F. Pan, *ACS Photonics* **2017**, *4*, 1344; c) C. F. Wang, R. R. Bao, K. Zhao, T. P. Zhang, L. Dong, C. F. Pan, *Nano Energy* **2015**, *14*, 364; d) R. R. Bao, C. F. Wang, L. Dong, C. Y. Shen, K. Zhao, C. F. Pan, *Nanoscale* **2016**, *8*, 8078.
- [48] a) N. Aristidou, I. Sanchez-Molina, T. Chotchuangchuchaval, M. Brown, L. Martinez, T. Rath, S. A. Haque, *Angew. Chem., Int. Ed.* **2015**, *54*, 8208; b) R. K. Misra, S. Aharon, B. Li, D. Mogilyansky, I. Visoly-Fisher, L. Etgar, E. A. Katz, *J. Phys. Chem. Lett.* **2015**, *6*, 326.
- [49] J. Wu, J. Chen, Y. Zhang, Z. Xu, L. Zhao, T. Liu, D. Luo, W. Yang, K. Chen, Q. Hu, *Nano Lett.* **2017**, *17*, 3563.
- [50] A. Baldan, *J. Mater. Sci.* **2002**, *37*, 2171.
- [51] J. Wu, F. Ye, W. Yang, Z. Xu, D. Luo, R. Su, Y. Zhang, R. Zhu, Q. Gong, *Chem. Mater.* **2018**, *30*, 4590.
- [52] C. H. Lin, Q. Zeng, E. Lafalce, S. Yu, M. J. Smith, Y. J. Yoon, Y. Chang, Y. Jiang, Z. Lin, Z. V. Vardeny, *Adv. Opt. Mater.* **2018**, *6*, 1800474.
- [53] C. Zou, C. Chang, D. Sun, K. F. Bohringer, L. Y. Lin, *Nano Lett.* **2020**, *20*, 3710.
- [54] a) J. Burschka, N. Pellet, S.-J. Moon, R. Humphry-Baker, P. Gao, M. K. Nazeeruddin, M. Grätzel, *Nature* **2013**, *499*, 316; b) K. Hwang, Y. S. Jung, Y. J. Heo, F. H. Scholes, S. E. Watkins, J. Subbiah, D. J. Jones, D. Y. Kim, D. Vak, *Adv. Mater.* **2015**, *27*, 1241.
- [55] H. Chen, *Adv. Funct. Mater.* **2017**, *27*, 1605654.
- [56] W. Wu, X. Wang, X. Han, Z. Yang, G. Gao, Y. Zhang, J. Hu, Y. Tan, A. Pan, C. Pan, *Adv. Mater.* **2019**, *31*, 1805913.
- [57] G. Wang, D. Li, H.-C. Cheng, Y. Li, C.-Y. Chen, A. Yin, Z. Zhao, Z. Lin, H. Wu, Q. He, *Sci. Adv.* **2015**, *1*, e1500613.
- [58] X. Liu, L. Niu, C. Wu, C. Cong, H. Wang, Q. Zeng, H. He, Q. Fu, W. Fu, T. Yu, *Adv. Sci.* **2016**, *3*, 1600137.
- [59] Y. Gao, L. Y. Zhao, Q. Y. Shang, Y. G. Zhong, Z. Liu, J. Chen, Z. P. Zhang, J. Shi, W. N. Du, Y. F. Zhang, S. L. Chen, P. Gao, X. F. Liu, X. N. Wang, Q. Zhang, *Adv. Mater.* **2018**, *30*, 1801805.
- [60] E. Oksenberg, E. Sanders, R. Popovitzbiro, L. Houben, E. Joselevich, *Nano Lett.* **2018**, *18*, 424.
- [61] a) M. Scheel, R. Seemann, M. Brinkmann, M. Di Michiel, A. Sheppard, B. Breidenbach, S. Herminghaus, *Nat. Mater.* **2008**, *7*, 189; b) M. Prakash, D. Quééré, J. W. Bush, *Science* **2008**, *320*, 931.
- [62] B. Pokroy, S. H. Kang, L. Mahadevan, J. Aizenberg, *Science* **2009**, *323*, 237.
- [63] J. Feng, X. Jiang, X. Yan, Y. Wu, B. Su, H. Fu, J. Yao, L. Jiang, *Adv. Mater.* **2017**, *29*, 1603652.
- [64] J. Feng, X. Yan, Y. Zhang, X. Wang, Y. Wu, B. Su, H. Fu, L. Jiang, *Adv. Mater.* **2016**, *28*, 3732.
- [65] J. Feng, C. Gong, H. Gao, W. Wen, Y. Gong, X. Jiang, B. Zhang, Y. Wu, Y. Wu, H. Fu, *Nat. Electron.* **2018**, *1*, 404.
- [66] a) M. Dong, I. Chatzis, *J. Colloid Interface Sci.* **1995**, *172*, 278; b) E. Kim, G. M. Whitesides, *J. Phys. Chem. B* **1997**, *101*, 855.
- [67] J. Feng, X. Yan, Y. Liu, H. Gao, Y. Wu, B. Su, L. Jiang, *Adv. Mater.* **2017**, *29*, 1605993.
- [68] W. Deng, L. Huang, X. Xu, X. Zhang, X. Jin, S.-T. Lee, J. Jie, *Nano Lett.* **2017**, *17*, 2482.
- [69] a) Z. Hu, M. Tian, B. Nysten, A. M. Jonas, *Nat. Mater.* **2009**, *8*, 62; b) S. J. Kang, Y. J. Park, J. Hwang, H. J. Jeong, J. S. Lee, K. J. Kim, H. C. Kim, J. Huh, C. Park, *Adv. Mater.* **2007**, *19*, 581; c) L. Chen, X. Wang, W. Lu, X. Wu, J. Li, *Chem. Soc. Rev.* **2016**, *45*, 2137.
- [70] B. Jeong, I. Hwang, S. H. Cho, E. H. Kim, S. Cha, J. Lee, H. S. Kang, S. M. Cho, H. Choi, C. Park, *ACS Nano* **2016**, *10*, 9026.
- [71] J. Mao, W. E. Sha, H. Zhang, X. Ren, J. Zhuang, V. A. Roy, K. S. Wong, W. C. Choy, *Adv. Funct. Mater.* **2017**, *27*, 1606525.
- [72] M. S. Alias, I. Dursun, D. Shi, M. I. Saidaminov, E. M. Diallo, D. Priante, T. K. Ng, O. M. Bakr, B. S. Ooi, *J. Vac. Sci. Technol., B* **2015**, *33*, 051207.
- [73] M. S. Alias, Y. Yang, T. K. Ng, I. Dursun, D. Shi, M. I. Saidaminov, D. Priante, O. M. Bakr, B. S. Ooi, *J. Phys. Chem. Lett.* **2016**, *7*, 137.
- [74] J. Fan, T. Wang, C. Yu, B. Tu, Z. Jiang, D. Zhao, *Adv. Mater.* **2004**, *16*, 1432.
- [75] Y. Gao, C. Huang, C. Hao, S. Sun, L. Zhang, C. Zhang, Z. Duan, K. Wang, Z. Jin, N. Zhang, *ACS Nano* **2018**, *12*, 8847.
- [76] a) B. Bao, M. Li, Y. Li, J. Jiang, Z. Gu, X. Zhang, L. Jiang, Y. Song, *Small* **2015**, *11*, 1649; b) M. Bag, Z. Jiang, L. A. Renna, S. P. Jeong, V. M. Rotello, D. Venkataraman, *Mater. Lett.* **2016**, *164*, 472.
- [77] Z. Gu, K. Wang, H. Li, M. Gao, L. Li, M. Kuang, Y. S. Zhao, M. Li, Y. Song, *Small* **2017**, *13*, 1603217.
- [78] a) M. Kuang, L. Wu, Y. Li, M. Gao, X. Zhang, L. Jiang, Y. Song, *Nanotechnology* **2016**, *27*, 184002; b) S. Feng, S. Wang, L. Gao, G. Li, Y. Hou, Y. Zheng, *Angew. Chem., Int. Ed.* **2014**, *53*, 6163.
- [79] J. Liu, B. Shabbir, C. Wang, T. Wan, Q. Ou, P. Yu, A. Tadich, X. Jiao, D. Chu, D. Qi, *Adv. Mater.* **2019**, *31*, 1901644.
- [80] M. I. Saidaminov, A. L. Abdelhady, B. Murali, E. Alarousu, V. M. Burlakov, W. Peng, I. Dursun, L. Wang, Y. He, G. Maculan, *Nat. Commun.* **2015**, *6*, 7586.
- [81] S. S. Chou, B. S. Swartzentruber, M. T. Janish, K. C. Meyer, L. B. Biedermann, S. Okur, D. B. Burckel, C. B. Carter, B. Kaehr, *J. Phys. Chem. Lett.* **2016**, *7*, 3736.
- [82] D. Tan, K. N. Sharafudeen, Y. Yue, J. Qiu, *Prog. Mater. Sci.* **2016**, *76*, 154.
- [83] a) Y. Shimotsuna, M. Sakakura, P. G. Kazansky, M. Beresna, J. Qiu, K. Miura, K. Hirao, *Adv. Mater.* **2010**, *22*, 4039; b) T. Fernandez, M. Sakakura, S. Eaton, B. Sotillo, J. Siegel, J. Solis, Y. Shimotsuna, K. Miura, *Prog. Mater. Sci.* **2018**, *94*, 68.
- [84] Y. Dong, H. Hu, X. Xu, Y. Gu, C.-C. Chueh, B. Cai, D. Yu, Y. Shen, Y. Zou, H. Zeng, *J. Phys. Chem. Lett.* **2019**, *10*, 4149.
- [85] X. Huang, Q. Guo, D. Yang, X. Xiao, X. Liu, Z. Xia, F. Fan, J. Qiu, G. Dong, *Nat. Photonics* **2020**, *14*, 82.
- [86] a) J. Michel, J. Liu, L. C. Kimerling, *Nat. Photonics* **2010**, *4*, 527; b) Y.-Y. Chen, C.-H. Wang, G.-S. Chen, Y.-C. Li, C.-P. Liu, *Nano Energy* **2015**, *11*, 533.
- [87] a) X. Dai, S. Zhang, Z. Wang, G. Adamo, H. Liu, Y. Huang, C. Couteau, C. Soci, *Nano Lett.* **2014**, *14*, 2688; b) D. Guo, Y. Su, H. Shi, P. Li, N. Zhao, J. Ye, S. Wang, A. Liu, Z. Chen, C. Li, *ACS Nano* **2018**, *12*, 12827.
- [88] a) C. Bao, J. Yang, S. Bai, W. Xu, Z. Yan, Q. Xu, J. Liu, W. Zhang, F. Gao, *Adv. Mater.* **2018**, *30*, 1803422; b) P. C. Chow, T. Someya, *Adv. Mater.* **2019**, 1902045; c) Y. Zhao, C. Li, L. Shen, *InfoMat* **2019**, *1*, 407.
- [89] a) S. Shrestha, R. Fischer, G. J. Matt, P. Feldner, T. Michel, A. Osvet, I. Levchuk, B. Merle, S. Golkar, H. Chen, *Nat. Photonics* **2017**, *11*, 436; b) W. Wei, Y. Zhang, Q. Xu, H. Wei, Y. Fang, Q. Wang, Y. Deng, T. Li, A. Gruverman, L. Cao, *Nat. Photonics* **2017**, *11*, 315; c) J. A. Steele, W. Pan, C. Martin, M. Keshavarz, E. Debroye, H. Yuan, S. Banerjee, E. Fron, D. Jonckheere, C. W. Kim, *Adv. Mater.* **2018**, *30*, 1804450.
- [90] a) S. D. Stranks, G. E. Eperon, G. Grancini, C. Menelaou, M. J. Alcocer, T. Leijtens, L. M. Herz, A. Petrozza,

- H. J. Snaith, *Science* **2013**, *342*, 341; b) Z.-K. Tan, R. S. Moghaddam, M. L. Lai, P. Docampo, R. Higler, F. Deschler, M. Price, A. Sadhanala, L. M. Pazos, D. Credgington, *Nat. Nanotechnol.* **2014**, *9*, 687; c) T. Fang, F. Zhang, S. Yuan, H. Zeng, J. Song, *InfoMat* **2019**, *1*, 211.
- [91] Y. Lei, Y. Chen, Y. Gu, C. Wang, Z. Huang, H. Qian, J. Nie, G. Hollett, W. Choi, Y. Yu, *Adv. Mater.* **2018**, *30*, 1705992.
- [92] a) Y. Fu, H. Zhu, A. W. Schrader, D. Liang, Q. Ding, P. Joshi, L. Hwang, X. Zhu, S. Jin, *Nano Lett.* **2016**, *16*, 1000; b) Y. Fu, H. Zhu, C. C. Stoumpos, Q. Ding, J. Wang, M. G. Kanatzidis, X. Zhu, S. Jin, *ACS Nano* **2016**, *10*, 7963.
- [93] Y. Nagaoka, K. Hills-Kimball, R. Tan, R. Li, Z. Wang, O. Chen, *Adv. Mater.* **2017**, *29*, 1606666.
- [94] M. D. Kelzenberg, S. W. Boettcher, J. A. Petykiewicz, D. B. Turner-Evans, M. C. Putnam, E. L. Warren, J. M. Spurgeon, R. M. Briggs, N. S. Lewis, H. A. Atwater, *Nat. Mater.* **2010**, *9*, 239.
- [95] T. Shegai, V. D. Miljkovic, K. Bao, H. Xu, P. Nordlander, P. Johansson, M. Kall, *Nano Lett.* **2011**, *11*, 706.
- [96] X. Gao, X. Zhang, W. Yin, H. Wang, Y. Hu, Q. Zhang, Z. Shi, V. L. Colvin, W. W. Yu, Y. Zhang, *Adv. Sci.* **2019**, *6*, 1900941.
- [97] a) S. D. Stranks, H. J. Snaith, *Nat. Nanotechnol.* **2015**, *10*, 391; b) H. Zhou, S. Yuan, X. Wang, T. Xu, X. Wang, H. Li, W. Zheng, P. Fan, Y. Li, L. Sun, *ACS Nano* **2017**, *11*, 1189.



Li Qiu received his M.E. and Ph.D. degrees in control theory and control engineering from the South China University of Technology, Guangzhou, China, in 2006 and 2011, respectively. Her current research interests include networked control systems, Markovian jump linear systems and robust control, and control of switched reluctance motors and generators.



Peiguang Yan received his Ph.D. degree from College of Physics Science, Nankai University, China, in 2005. He joined the Shenzhen University, China, in 2005 as a lecturer, and became an associate professor (2007–2012) and was promoted to professor from 2013. His current research interests include fiber optics, ultrafast fiber lasers, fiber sensors, and silicon photonics.



Caofeng Pan received his B.Sc. degree (2005) and Ph.D. (2010) degree in materials science and engineering from Tsinghua University, China. Then, he joined the group of Prof. Zhong Lin Wang at the Georgia Institute of Technology as a postdoctoral fellow. He has been a professor and a group leader at the Beijing Institute of Nanoenergy and Nanosystems, Chinese Academy of Sciences since 2013. His research interests mainly focus on the fields of piezotronics/piezophotonics for fabricating new electronic and optoelectronic devices, nanopower sources, hybrid nanogenerators, and self-powered nanosystems.